View metadata, citation and similar papers at core.ac.uk
brought to you by CORE
provided by NASA Technical Reports Server

NASA/TM—2012-217212
AHS2011–000178

Variable-Speed Simulation of a Dual-Clutch Gearbox Tiltrotor Driveline

Hans DeSmidt
University of Tennessee, Knoxville, Tennessee

Kon-Well Wang
University of Michigan, Ann Arbor, Michigan

Edward C. Smith
Penn State University, University Park, Pennsylvania

David G. Lewicki
Glenn Research Center, Cleveland, Ohio

January 2012

NASA STI Program . . . in Profile

Since its founding, NASA has been dedicated to the advancement of aeronautics and space science. The NASA Scientific and Technical Information (STI) program plays a key part in helping NASA maintain this important role.

The NASA STI Program operates under the auspices of the Agency Chief Information Officer. It collects, organizes, provides for archiving, and disseminates NASA's STI. The NASA STI program provides access to the NASA Aeronautics and Space Database and its public interface, the NASA Technical Reports Server, thus providing one of the largest collections of aeronautical and space science STI in the world. Results are published in both non-NASA channels and by NASA in the NASA STI Report Series, which includes the following report types:

- TECHNICAL PUBLICATION. Reports of completed research or a major significant phase of research that present the results of NASA programs and include extensive data or theoretical analysis. Includes compilations of significant scientific and technical data and information deemed to be of continuing reference value. NASA counterpart of peer-reviewed formal professional papers but has less stringent limitations on manuscript length and extent of graphic presentations.

- TECHNICAL MEMORANDUM. Scientific and technical findings that are preliminary or of specialized interest, e.g., quick release reports, working papers, and bibliographies that contain minimal annotation. Does not contain extensive analysis.

- CONTRACTOR REPORT. Scientific and technical findings by NASA-sponsored contractors and grantees.

- CONFERENCE PUBLICATION. Collected papers from scientific and technical conferences, symposia, seminars, or other meetings sponsored or cosponsored by NASA.

- SPECIAL PUBLICATION. Scientific, technical, or historical information from NASA programs, projects, and missions, often concerned with subjects having substantial public interest.

- TECHNICAL TRANSLATION. English-language translations of foreign scientific and technical material pertinent to NASA's mission.

Specialized services also include creating custom thesauri, building customized databases, organizing and publishing research results.

For more information about the NASA STI program, see the following:

- Access the NASA STI program home page at *http://www.sti.nasa.gov*

- E-mail your question via the Internet to *help@sti.nasa.gov*

- Fax your question to the NASA STI Help Desk at 443–757–5803

- Telephone the NASA STI Help Desk at 443–757–5802

- Write to:
  NASA Center for AeroSpace Information (CASI)
  7115 Standard Drive
  Hanover, MD 21076–1320

NASA/TM—2012-217212 AHS2011–000178

Variable-Speed Simulation of a Dual-Clutch Gearbox Tiltrotor Driveline

Hans DeSmidt
University of Tennessee, Knoxville, Tennessee

Kon-Well Wang
University of Michigan, Ann Arbor, Michigan

Edward C. Smith
Penn State University, University Park, Pennsylvania

David G. Lewicki
Glenn Research Center, Cleveland, Ohio

Prepared for the
67th Annual Forum and Technology Display (Forum 67)
sponsored by the American Helicopter Society (AHS)
Virginia Beach, Virginia, May 3–5, 2011

National Aeronautics and
Space Administration

Glenn Research Center
Cleveland, Ohio 44135

January 2012

Acknowledgments

This work was supported under NASA Grant no. NNX07AC58A, with
Technical Monitors Dr. Robert F. Handschuh and Dr. David G. Lewicki.

Trade names and trademarks are used in this report for identification only. Their usage does not constitute an official endorsement, either expressed or implied, by the National Aeronautics and Space Administration.

Level of Review: This material has been technically reviewed by technical management.

Available from

NASA Center for Aerospace Information
7115 Standard Drive
Hanover, MD 21076–1320

National Technical Information Service
5301 Shawnee Road
Alexandria, VA 22312

Available electronically at http://www.sti.nasa.gov

Variable-Speed Simulation of a Dual-Clutch Gearbox Tiltrotor Driveline

Hans DeSmidt
University of Tennessee
Knoxville, Tennessee 37996

Kon-Well Wang
University of Michigan
Ann Arbor, Michigan 48109-2125

Edward C. Smith
Penn State University
University Park, Pennsylvania 16802

David G. Lewicki
National Aeronautics and Space Administration
Glenn Research Center
Cleveland, Ohio 44135

Abstract

This investigation explores the variable-speed operation and shift response of a prototypical two-speed dual-clutch transmission tiltrotor driveline in forward flight. Here, a Comprehensive Variable-Speed Rotorcraft Propulsion System Modeling (CVSRPM) tool developed under a NASA funded NRA program is utilized to simulate the drive system dynamics. In this study, a sequential shifting control strategy is analyzed under a steady forward cruise condition. This investigation attempts to build upon previous variable-speed rotorcraft propulsion studies by 1) including a fully nonlinear transient gas-turbine engine model, 2) including clutch stick-slip friction effects, 3) including shaft flexibility, 4) incorporating a basic flight dynamics model to account for interactions with the flight control system. Through exploring the interactions between the various subsystems, this analysis provides important insights into the continuing development of variable-speed rotorcraft propulsion systems.

Introduction

According to a recent NASA-Army-Industry-University investigation, significant benefits to rotorcraft operational performance, effectiveness and acoustic signature could be gained through the ability to adjust main rotor speed to accommodate various flight conditions (Ref. 1). In particular, variable-speed rotor technology is critical to the slowed-rotor compound configuration concepts and would offer significant benefits to future Heavy-Lift helicopter and tiltrotor configurations (Ref. 2). Current rotorcraft propulsion systems are designed around a fixed-ratio transmission without the capability to vary rotor speed except by engine speed adjustment. Since the specific fuel consumption of modern gas-turbine engines is optimum within a relatively narrow speed range, the ability to achieve a variable-speed rotor through engine speed adjustment is limited (Refs. 3 and 4). Therefore, to achieve effective variable rotor speed designs, a variable ratio transmission in the rotorcraft propulsion system becomes attractive. The NASA Heavy-Lift study (Ref. 1) suggests that transmission designs capable of rotor speed variations on the order of 50 percent will be sufficient to achieve significant rotorcraft performance and noise benefits.

Recently, Stevens, Handschuh, and Lewicki (Ref. 5) presented several variable and multi-speed rotorcraft drive system concepts. Based on relative simplicity and necessary requirements of positive drive (i.e., no traction or fluid-based power transmission) for rotorcraft applications, it was concluded that one promising configuration would incorporate a planetary drive with a discrete two-speed shift capability. Therefore, a two-speed dual-clutch planetary gear transmission of the type evaluated by Lewicki, et al. (Ref. 6) is considered in the current investigation. In Lewicki, et al. (Ref. 6), a model and analysis of the dual-clutch shifting dynamics including nonlinear dry clutch stick-slip friction and dual-clutch control is developed and experimentally validated on a purpose-built test rig at the NASA Glenn Research Center. Furthermore, the shift dynamics of similar dual-clutch transmissions for automotive applications were explored (Refs. 7 and 8). One advantage offered by dual-clutch transmissions (DCT) is their ability to provide continuous power transfer when transitioning from one gear ratio to another. Depending on the dual-clutch shift control strategy, a pure neutral condition can be avoided during the shifting process, a seeming obvious benefit for rotorcraft applications. Generally speaking, to accommodate a gear ratio change, it is kinematically necessary for either the engine speed or the load speed to vary. For example, during an upshift from a lower gear to a higher gear, either the load speed must increase or the engine RPM must decrease (or some combination therein). In automotive systems, since the engine rotary inertia is typically much lower that the effective vehicle inertia, the engine speed primarily changes during clutch engagement.

Once clutch lockup in the new gear ratio occurs, the engine speed is then adjusted to obtain the desired vehicle speed.

In the case of rotorcraft, since it is important to maintain powered flight throughout the shift process and not to over-speed the engine power turbines, Litt, et al. (Ref. 9) proposed an engine-at-a-time or sequential shifting control (SSC) for multi engine helicopters. This approach takes advantage of the existing drive system free-wheeling clutch connections to decouple individual engines from the transmission thus allowing sequential gear ratio changes on individual transmission paths. In particular, Litt, et al. (Ref. 9) explored this concept for a 3000 hp class, two-engine single rotor helicopter using an integrated system model consisting of a linearized engine, rigid gear transmission, rotor and idealized clutches to capture the basic dynamics. The advantages of this approach are that: 1) it allows for powered flight to always be maintained on the reduced set of engines, and 2) it avoids full power transfer across engaging clutches.

The purpose of the current investigation is to explore the variable-speed operation and shift response of a prototypical two-speed DCT tiltrotor driveline in forward flight airplane mode. Here, a Comprehensive Variable-Speed Rotorcraft Propulsion System Modeling (CVSRPM) tool developed under a NASA-funded NRA program is utilized to simulate the drive system dynamics under a two-speed shift SSC strategy for several mission scenarios.

As discussed in References 1, 3, and 4, one of the potential beneficiaries of variable-speed rotor drive-system technologies is Heavy-Lift rotorcraft. Therefore, this study considers a two-speed version of the 30,000 hp-class NASA Large Civil Tiltrotor Iteration 2 (LCTR-2) (Fig. 1, (Ref. 4)) and analyzes the transition to and from slowed rotor cruise operation. The simulations in this paper include a stick-slip dry clutch friction DCT model based on Lewicki, et al. (Ref. 6), a new fully nonlinear first principles-based transient gas turbine engine model, cross shaft flexibility effects, and an idealized uniform inflow forward flight rotor/propeller model.

Figure 1.—NASA Large Civil Tiltrotor LCTR-2 (Ref. 4).

Two-Speed Tiltrotor Simulation

A schematic of the two-speed dual-path tiltrotor driveline considered in this investigation is shown in Figure 2. Each path consists of an engine nacelle containing a pair of gas turbine engines coupled to an initial reduction gearbox, ratio n_i, via freewheeling clutch units (FWU), see Appendix A, Nomenclature.

$$n_i = \frac{\Omega_{DCT,\mathrm{in}}}{\Omega_{FWU,\mathrm{out}}} = 1.87:1 \tag{1}$$

Speed is then further reduced by a two-speed DCT gearbox with low and high ratios

$$n_{DCT,\mathrm{low}} = \frac{\Omega_{DCT,\mathrm{low}}}{\Omega_{DCT,\mathrm{in}}} = 0.383\ ,\ n_{DCT,\mathrm{high}} = \frac{\Omega_{DCT,\mathrm{high}}}{\Omega_{DCT,\mathrm{in}}} = 0.71 \tag{2}$$

The final reduction, ratio n_f, before the main rotor is represented as a high reduction ratio planetary gearbox

$$n_f = \frac{\Omega_{MR}}{\Omega_{DCT}} = 25:1 \tag{3}$$

Finally, the left and right side driveline paths are linked via a cross-shaft.

The cross-shaft is located downstream from the DCT speed changing units (see Fig. 2) to prevent relative rotor windup during shift events thus ensuring that rotor indexing phase is maintained.

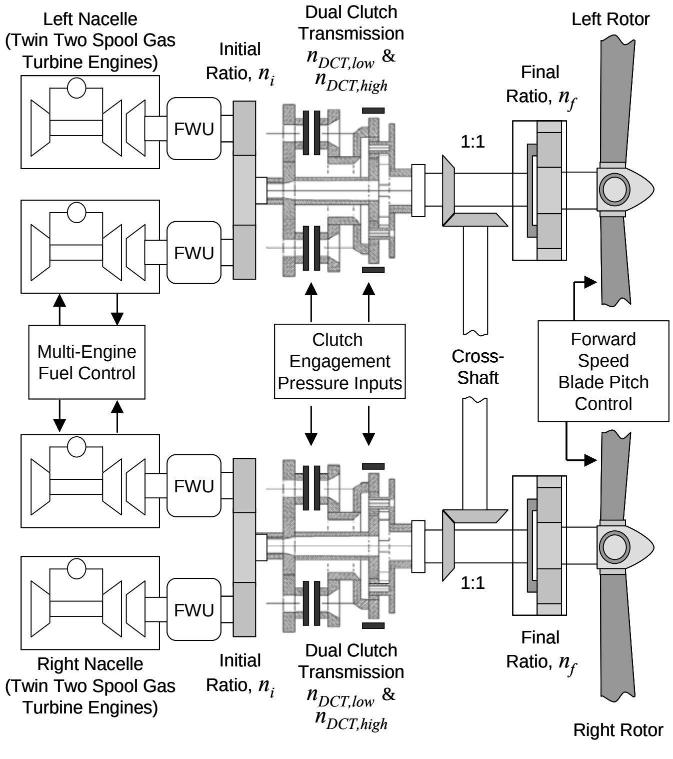

Left Nacelle (Twin Two Spool Gas Turbine Engines)
Initial Ratio, n_i
Dual Clutch Transmission $n_{DCT,low}$ & $n_{DCT,high}$
Left Rotor
Final Ratio, n_f
FWU
FWU
1:1
Multi-Engine Fuel Control
Clutch Engagement Pressure Inputs
Cross-Shaft
Forward Speed Blade Pitch Control
FWU
FWU
1:1
Right Nacelle (Twin Two Spool Gas Turbine Engines)
Initial Ratio, n_i
Dual Clutch Transmission $n_{DCT,low}$ & $n_{DCT,high}$
Final Ratio, n_f
Right Rotor

Figure 2.—Two-speed DCT dual-path tiltrotor driveline.

To simulate forward flight operation, the propulsion system model is coupled to a simplified flight dynamics block to account for vehicle altitude and forward speed regulation under variable rotor speed operation. Since all engines were considered to be identical, only one engine-per-side was simulated in the model, with appropriate output torque and inertia effects to account for both engines. Figure 3 shows the architecture of the overall propulsion system coupled with a vehicle flight dynamics block and associated closed-loop flight control systems and command inputs.

A description of the main elements and some key assumptions included in the simulation model are as follows:

- Two-spool gas turbine engine transient dynamics model with closed-loop PID-based fuel controller to regulate power turbine speed Ω_{pt} and multi-engine load sharing.
- DCT model with nonlinear stick-slip friction and clutch lockup effects and open loop clutch engagement pressure command inputs (Ref. 6).
- Idealized rigid gearing (tooth meshing compliance neglected).
- Main rotor idealized as rigid rotational inertia with aerodynamic torque computed based on momentum theory with uniform inflow (Ref. 10).
- Torsionally flexible cross-shafting.
- Simplified vehicle flight dynamics model with horizontal and vertical degrees of freedom (two DOF) accounting for fuselage drag, vehicle weight, rotor thrust and wing lift.
- A PID-based main rotor blade pitch controller to regulate rotor thrust and track a desired forward speed set-point (controls main rotor pitch θ_p).
- A PID-based wing elevon pitch controller to maintain flight level or track a desire climb rate set-point (controls wing flap angle θ_w).

The simulation model was developed in the Matlab Simulink (The MathWorks, Inc.) environment. Appendix B shows the system and subsystem block diagrams. Further details of the propulsion system model are given in the subsequent subsections.

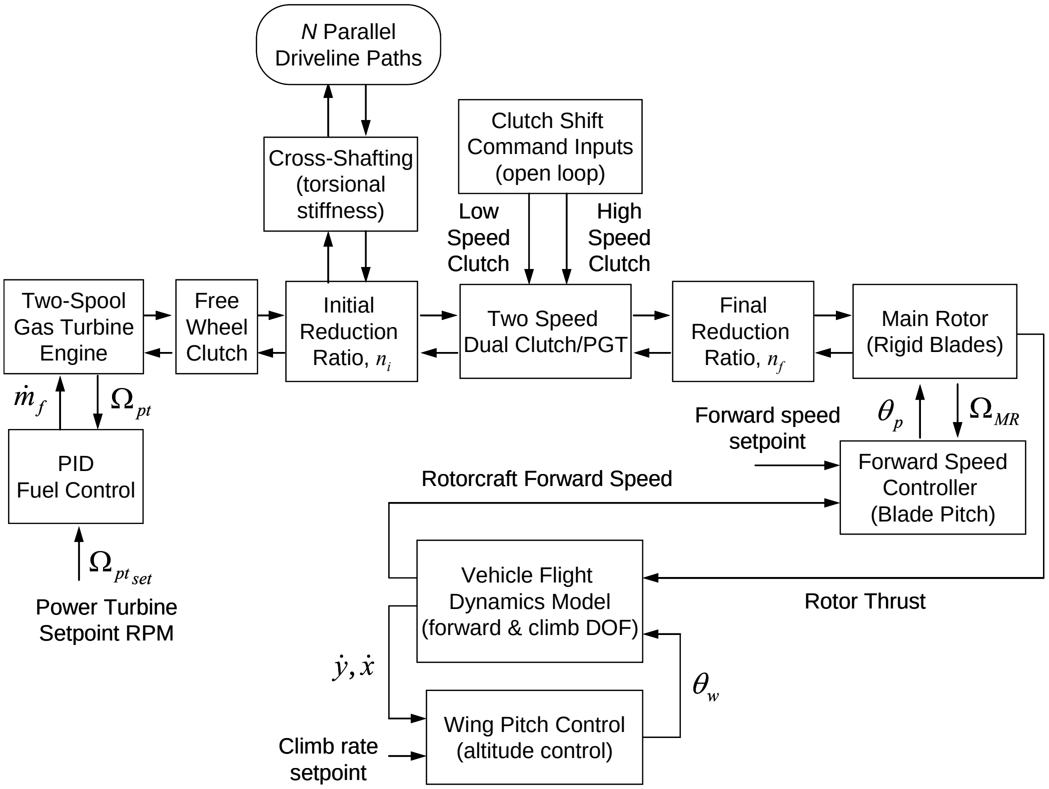
N Parallel Driveline Paths
Cross-Shafting (torsional stiffness)
Clutch Shift Command Inputs (open loop)
Low Speed Clutch
High Speed Clutch
Two-Spool Gas Turbine Engine
Free Wheel Clutch
Initial Reduction Ratio, n_i
Two Speed Dual Clutch/PGT
Final Reduction Ratio, n_f
Main Rotor (Rigid Blades)
$\dot{m}_f$
Ω_{pt}
PID Fuel Control
$\Omega_{pt_{set}}$
Power Turbine Setpoint RPM
Forward speed setpoint
θ_p
Ω_{MR}
Forward Speed Controller (Blade Pitch)
Rotorcraft Forward Speed
Vehicle Flight Dynamics Model (forward & climb DOF)
Rotor Thrust
$\dot{y}, \dot{x}$
θ_w
Wing Pitch Control (altitude control)
Climb rate setpoint

Figure 3.—Propulsion system/vehicle dynamics/flight control block diagram assembled in the CVSRPM code.

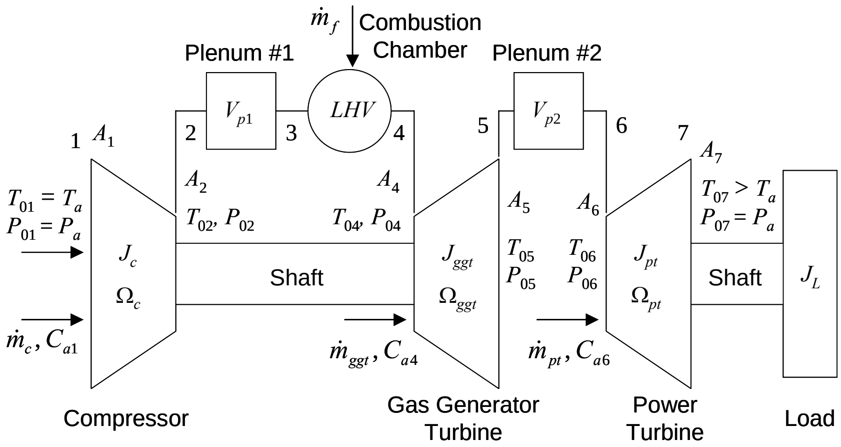

Figure 4.—Two-spool gas turbine engine model components and analysis stations.

Gas Turbine Engine Model

To model the gas turbine engines and fuel control dynamics during transient operation, a generic two-spool gas turbine engine model was developed. The components of this model, shown in Figure 4, include the axial compressor, combustion chamber, gas-generator turbine, power turbine and two mass accumulators (plenums). A dynamic model is formulated by considering the torque balances between the compressor and gas generator turbine as well as between the power turbine and load. These torques are computed based on first principles mechanical and thermodynamic laws following a similar approach as in reference (Ref. 6). The thermodynamic model is based on the standard Joule/Brayton cycle (Ref. 11). The main assumptions made in this analytical model can be summarized as follows:

Engine model assumptions:

- The air mass flows through the system are all one-dimensional at the mean line.
- Air with ideal gas law behavior is assumed.
- All expansion and compression is adiabatic.
- The inlet stagnation temperature and pressures are constant.
- All power transfer occurs in the rotor stages, the stators do no work.
- The instantaneous compressor mass flow, pressure ratio and efficiency are determined via pre-calculated beta maps.
- Gas generator and power turbines are in a state of choking flow (Ref. 11)
- No air bleed occurs from the compressor.
- The combustion is modeled as isobaric heat addition.
- The specific heat of air was assumed constant throughout the engine model.

The power required to drive the compressor is

$$W_c = \dot{m}_c c_p (T_{02} - T_{01}) \tag{4}$$

Where $\dot{m}_c$ is the compressor air mass flow rate, c_p is the specific heat of air and T_{01} and T_{02} are the stagnation temperatures at the compressor entrance and exit respectively. Furthermore the stagnation temperature ratio is related to the compressor pressure ratio by

$$\frac{T_{02}}{T_{01}} = 1 + \frac{1}{\eta_c}\left[\left(\frac{P_{02}}{P_{01}}\right)^{\frac{\gamma-1}{\gamma}} - 1\right] \tag{5}$$

Where η_c is the compressor isentropic efficiency, γ is the specific heat ratio, and P_{01} and P_{02} are the stagnation pressures at the compressor entrance and exit respectively. Based on (4) and (5), the torque required to drive the compressor is

$$TQ_c = J_c\dot{\Omega}_c + \dot{m}_c c_p \frac{T_{01}}{\Omega_c \eta_c}\left[\left(\frac{P_{02}}{P_{01}}\right)^{\frac{\gamma-1}{\gamma}} - 1\right] \tag{6}$$

Where Ω_c is the compressor rotation speed and J_c is compressor rotational inertia. Also, in the above equations the stagnation temperature and pressures at the compressor entrance are assumed to be the ambient atmospheric pressure, $P_{01}=P_a$, and temperature $T_{01} = T_a$ values.

The basic engine parameters, summarized in Table 1, are selected based on the NASA LCTR-2 heavy lift concept engine prototype (Refs. 12 and 13).

TABLE 1.—ENGINE NOMINAL PARAMETERS

Parameter	Value
Ambient temperature, T_a	288° K
Ambient pressure, P_a	1.023 bar
Nominal output (load) power, W_L	7500 hp
Nominal compressor mass flow, $\dot{m}_{cn}$	13.5 kg/s
Nominal compressor pressure ratio, pr_{cn}	28
Nominal compressor axial velocity, C_{an}	150 m/s
Number of compressor stages, N_s	8
Compressor mean radius, R_c	0.119 m
Compressor inlet hub-to-tip ratio, ht_c	0.35
Nominal compressor speed, Ω_{cn}	26,500 RPM
Power turbine mean radius, R_{pt}	0.1811 m
Power turbine inlet hub-to-tip ratio, ht_{pt}	0.65
Nominal power turbine speed, Ω_{ptn}	12,500 RPM
Compressor rotational inertia, J_c	0.641 kg m^2
Gas generator turbine rotational inertia, J_{ggt}	0.144 kg m^2
Power turbine rotational inertia, J_{pt}	1.04 kg m^2
Plenum chamber volume, V_p	0.1 m^3
Combustion chamber loss coefficient, η_{cc}	0.85
Combustion chamber time constant, τ_{cc}	5.0×10^{-4} sec
Fuel lower heating value, LHV	43.1 MJ/kg
Nominal fuel rate, $\dot{m}_{fn}$	0.225 kg/sec
Maximum fuel rate, $\dot{m}_{f\max}$	0.338 kg/sec

Furthermore, the compressor mass flow rate, $\dot{m}_c$, pressure ratio, pr_c, and efficiency characteristics, η_c, are computed by way of so-called beta maps (Ref. 14) with functional dependencies,

$$
\begin{aligned}
pr_c &= f_{pr}(T_a, P_a, \Omega_c, \beta_c) \\
\dot{m}_c &= f_m(T_a, P_a, \Omega_c, \beta_c) \\
\eta_c &= f_\eta(T_a, P_a, \Omega_c, \beta_c)
\end{aligned}
\qquad (7\text{-a})
$$

Where β_c is the compressor beta parameter which maps the mass flow to pressure ratio as

$$pr_c = \beta_c \dot{m}_c^{\,2} \qquad (7\text{-b})$$

In this study, the compressor pressure and efficiency maps are generated numerically based on the nominal compressor design values. Figure 5 shows the pressure-ratio versus mass flow characteristic curves and beta lines for the 7500 hp gas turbine engine considered in this study and Figure 6 shows the compressor adiabatic efficiencies η_c.

To drive the compressor and load, separate gas generator and power turbines are present in the two-spool gas turbine engine (Fig. 4). The power generated from these turbines is

$$W_{ggt} = \dot{m}_{ggt} c_p (T_{04} - T_{05}) \text{ and } W_{pt} = \dot{m}_{pt} c_p (T_{06} - T_{07}) \qquad (8)$$

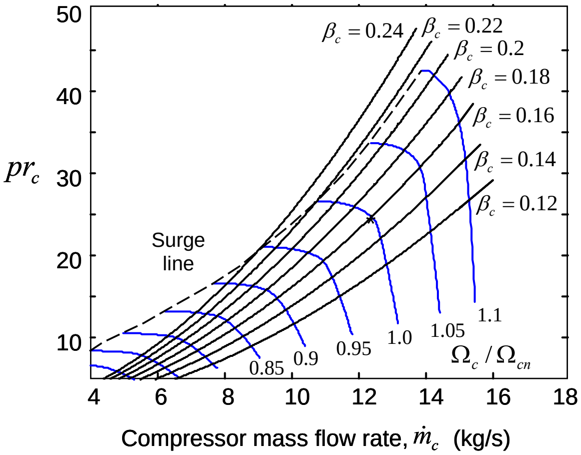

Figure 5.—Compressor pressure ratio versus air mass flow.

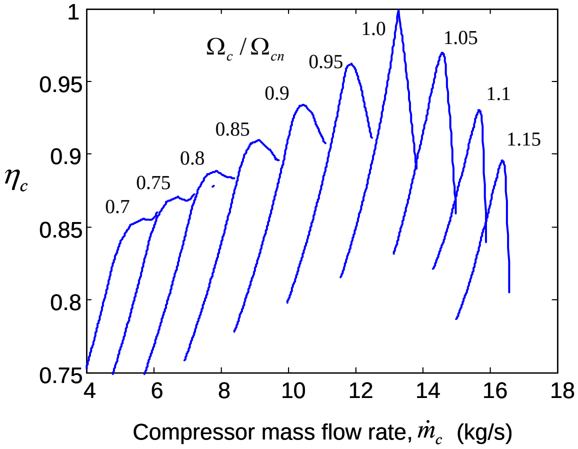

Figure 6.—Compressor adiabatic efficiency vs. mass flow.

Where $\dot{m}_{ggt}$ and $\dot{m}_{pt}$ are gas generator and power turbine mass flows, respectively, and T_{04}, T_{05}, T_{06} and T_{07} are turbine entrance and exit stagnation temperatures as defined in Figure 4. Furthermore, the turbine pressure ratios based on isentropic expansion thought the turbines are

$$\frac{P_{04}}{P_{05}} = \left(\frac{T_{04}}{T_{05}}\right)^{\frac{\gamma}{\gamma-1}} \text{ and } \frac{P_{06}}{P_{07}} = \left(\frac{T_{06}}{T_{07}}\right)^{\frac{\gamma}{\gamma-1}} \qquad (9)$$

and the turbine mass flows are computed based on the assumption that both turbines are operating in the condition of choking flow (Ref. 11). Therefore

$$\dot{m}_{ggt} = \varphi \frac{A_4 P_{04}}{\sqrt{T_{04}}} \text{ and } \dot{m}_{pt} = \varphi \frac{A_6 P_{06}}{\sqrt{T_{06}}} \qquad (10\text{-a})$$

with

$$\varphi \equiv \sqrt{\frac{\gamma}{R}\left(1+\frac{\gamma-1}{2}\right)^{\frac{\gamma+1}{1-\gamma}}} \qquad \text{(10-b)}$$

Where R is the ideal gas constant. Next, since the gas generator turbine and compressor are on a common spool, we have $\Omega_c = \Omega_{ggt}$, Also, the torque difference between the compressor and gas generator turbine is

$$(J_c + J_{ggt})\dot{\Omega}_c = \frac{1}{\Omega_c}(W_{ggt} - W_c) \qquad \text{(11)}$$

and the torque difference between power turbine and load is

$$(J_{pt} + J_L)\dot{\Omega}_{pt} = \frac{1}{\Omega_{pt}}(W_{pt} - W_L) \qquad \text{(12)}$$

Where W_L is the power consumed by the load and J_c , J_{ggt}, J_{pt} and J_L are rotational inertias of the compressor, gas generator turbine, power turbine, and the load, respectively.

During steady-state operation the air mass flow rates through the compressor and turbines are equal, $\dot{m}_c = \dot{m}_{ggt} = \dot{m}_{pt}$. However, during transient operation, differential mass flows can develop between the components due to volume packing (Refs. 14 and 15). To account for such transient effects, two plenum chambers (Plenum no. 1, situated between compressor and combustion chamber, and Plenum no. 2 between the two turbine units) are included in the model as depicted in Figure 4.

The plenum chambers are modeled as ideal mass accumulators with no losses or heat transfer. Figure 7 shows a schematic of the plenum chamber element with input and output mass flow rates $\dot{m}_{\text{in}}$ and $\dot{m}_{\text{out}}$ generated by the upstream and downstream elements. Due to the differential mass flows, the rate of change of density inside a plenum, $\dot{\rho}_p$, is given by

$$\dot{\rho}_p = \frac{\dot{m}_{\text{in}} - \dot{m}_{\text{out}}}{V_p} \qquad \text{(13)}$$

Where V_p is plenum chamber volume. Furthermore, through differentiation of the ideal gas law and assuming adiabatic compression, the following differential equation for plenum chamber pressure P_p is obtained

$$\dot{P}_p(t) = \frac{\gamma(\dot{m}_{\text{in}} - \dot{m}_{\text{out}})}{m_{pa}(t)} P_p(t) \qquad \text{(14-a)}$$

with

$$m_{pa}(t) = \int (\dot{m}_{\text{in}} - \dot{m}_{\text{out}})dt + m_{pa0} \qquad \text{(14-b)}$$

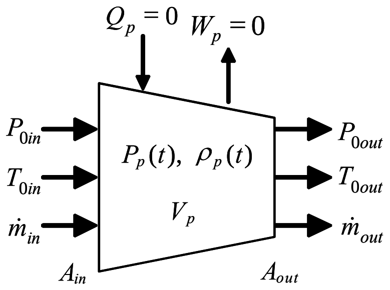

Figure 7.—Plenum chamber element.

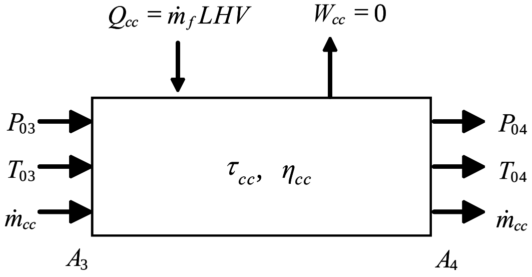

Figure 8.—Combustion chamber element.

Here m_{pa} is the mass of air accumulating inside the plenum and m_{pa0} is the initial air mass.

It is assumed that plenum pressure is uniform throughout its volume and that velocity effects and energy accumulation inside the plenum are negligible resulting in

$$P_{0\text{in}} = P_p \text{ and } P_{0\text{out}} = P_p \qquad \text{(15)}$$

and

$$T_{0\text{in}} = T_{0\text{out}} \qquad \text{(16)}$$

Where $P_{0\text{in}}$, and $P_{0\text{out}}$ are plenum entrance and exit stagnation pressures and $T_{0\text{in}}$, and $T_{0\text{out}}$ are the plenum entrance and exit stagnation temperatures.

Finally, the combustion chamber (entrance station 3, exit station 4 in Figs. 4 and 8) is modeled as a pure isobaric heat addition process. With heat addition, Q_{cc}, based on the idealized combustion model

$$Q_{cc} = \dot{m}_f LHV \qquad \text{(17)}$$

Where $\dot{m}_f$ is fuel mass flow rate and LHV is the fuel lower heating value.

As a result of an energy balance, the combustion chamber exit stagnation temperature T_{04} is determined as a solution to

$$\tau_{cc}\frac{dT_{04}}{dt} = \dot{m}_{cc}c_p(T_{03} - T_{04}) + \dot{m}_f LHV \qquad \text{(18)}$$

Where τ_{cc} is the combustion chamber time-constant and $\dot{m}_{cc}$ is the air mass flow through the combustion chamber which equals the mass flow drawn by the gas generator turbine $\dot{m}_{cc} = \dot{m}_{ggt}$. Furthermore, the combustion chamber exit stagnation pressure, P_{04}, is computed from the input stagnation pressure P_{03} using,

$$P_{04} = \eta_{cc} P_{03} \tag{19}$$

Where $\eta_{cc} < 1$ is the combustion chamber pressure drop ratio. Also, at steady-state the combustion temperature rise $\Delta T_{0cc} = T_{04} - T_{03}$ is

$$\Delta T_{0cc} = f \frac{LHV}{c_p} \text{ with } f = \frac{\dot{m}_f}{\dot{m}_{cc}} \tag{20}$$

Where f is the fuel-air ratio. Based on the equations presented in this subsection, the transient response of the two-spool gas turbine engine can be simulated. Please refer to the Appendix B for the full engine model block diagrams.

Dual-Clutch Gearbox Model

As mentioned in the previous section, a two-speed DCT gearbox is utilized as the ratio changing element in each transmission path of the tiltrotor drive system (Fig. 2). A schematic of the DCT considered in this study is shown in Figure 9 along with the corresponding kinematic diagram in Figure 10. Here the carrier is the output. In the DCT, high ratio, $n_{DCT,high}$ is achieved by engaging the multiple clutch disks that couple the planet shafts (clutch 1).

$$n_{DCT,\text{high}} = \frac{Z_i Z_{cg2} Z_r}{2(Z_{cg1} Z_{cg3} + Z_s)(Z_p + Z_s)} \tag{21-a}$$

Furthermore, low ratio, $n_{DCT,low}$, is achieved by fully engaging, a cylindrical clutch (clutch 2) which clamps the ring gear.

$$n_{DCT,\text{low}} = \frac{Z_s}{2(Z_p + Z_s)} \tag{21-b}$$

Clutch engagement is controlled by applied pressures, p_{cl1} and p_{cl2}, normal to the clutch fiction surfaces. Due to the DCT kinematics, the only condition under which both sets of clutches can be engaged and locked simultaneously corresponds to the zero speed or fully stalled condition. When both clutches are applied simultaneously there is a negative recirculating power ratio and clutches act as a braking system. Thus, during steady-state constant speed operation, only one clutch is fully engaged and locked ($p_{cli} = p_{cl\max}$) while the other clutch remains open ($p_{clj} = 0$).

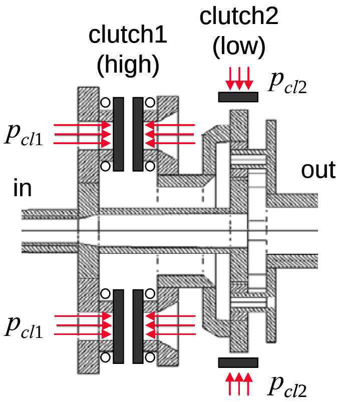

Figure 9.—Dual-clutch transmission.

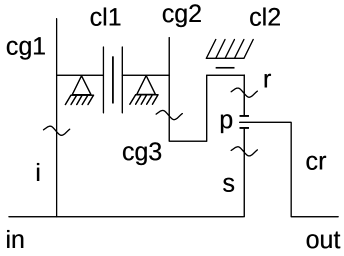

Symbol	Component
i	input gear
cg1, cg2 & cg3	control gears
r	ring
p	planet
s	sun
cr	carrier
cl1 & cl2	clutch 1 & 2
~	gear mesh

Figure 10.—DCT kinematic diagram.

To account for the DCTs in the driveline simulation, a rigid body dynamics model is developed which accounts for the DCT kinematics, the gear rotational inertias, and the nonlinear clutch friction torques.

$$\mathbf{M}\ddot{\mathbf{q}} = \mathbf{F}(\ddot{\mathbf{q}}, \dot{\mathbf{q}}, p_{cl1}, p_{cl2}) \tag{22-a}$$

with corresponding DOF vector

$$\mathbf{q}(t) = [\phi_i,\ \phi_r]^T \tag{22-b}$$

Where ϕ_i and ϕ_r are the DCT input and ring gear rotations. Also, the system inertia matrix is given by

$$\mathbf{M} = \begin{bmatrix} \begin{array}{l} J_{in} + J_i + J_s + \dfrac{J_{cg1} N_{cg} Z_i^{\;2}}{Z_{cg1}^{\;2}} + \ldots \\ \dfrac{Z_s^{\;2}}{4}\left(\dfrac{J_{cr} + J_{out} + N_p m_p R_{cr}^{\;2}}{(Z_p + Z_s)^2} + \dfrac{J_p N_p}{Z_p^{\;2}} \right) \end{array} & \dfrac{Z_r Z_s}{4}\left(\dfrac{J_{cr} + J_{out} + N_p m_p R_{cr}^{\;2}}{(Z_p + Z_s)^2} - \dfrac{J_p N_p}{Z_p^{\;2}} \right) \\ \dfrac{Z_r Z_s}{4}\left(\dfrac{J_{cr} + J_{out} + N_p m_p R_{cr}^{\;2}}{(Z_p + Z_s)^2} - \dfrac{J_p N_p}{Z_p^{\;2}} \right) & \begin{array}{l} J_r + J_{cg3} + \dfrac{J_{cg2} N_{cg} Z_{cg3}^{\;2}}{Z_{cg2}^{\;2}} + \ldots \\ \dfrac{Z_r^{\;2}}{4}\left(\dfrac{J_{cr} + J_{out} + N_p m_p R_{cr}^{\;2}}{(Z_p + Z_s)^2} + \dfrac{J_p N_p}{Z_p^{\;2}} \right) \end{array} \end{bmatrix} \tag{22-c}$$

and the system generalized force vector is

$$\mathbf{F} = \begin{bmatrix} 1 & \dfrac{-Z_s}{2(Z_p + Z_s)} & \dfrac{-N_{cg} Z_i}{Z_{cg1}} & 0 \\ 0 & \dfrac{-Z_r}{2(Z_p + Z_s)} & \dfrac{N_{cg} Z_{cg3}}{Z_{cg2}} & -1 \end{bmatrix} \begin{bmatrix} TQ_{\text{in}} \\ TQ_{\text{out}} \\ TQ_{cl1} \\ TQ_{cl2} \end{bmatrix} \tag{22-d}$$

Where TQ_{in} and TQ_{out} are the torques on the DCT input and output shafts and where TQ_{cl1} and TQ_{cl2} are the transmitted clutch torques. To account for the possibility of clutch sticking (lock-up) or slipping, the clutch torques are computed based on a so-called combined Coulomb / viscous model (Refs. 6, 16, and 17)

$$TQ_{cl1} = \begin{cases} \tau_{cl}(\Omega_{cg2} - \Omega_{cg1}) & \left|\Omega_{cg2} - \Omega_{cg1}\right| < \varepsilon \\ p_{cl1}\mu_{cl}\dfrac{4\pi\, R_{cl1}^{\;3}}{3}\operatorname{sgn}(\Omega_{cg2} - \Omega_{cg1}) & \left|\Omega_{cg2} - \Omega_{cg1}\right| \geq \varepsilon \end{cases} \tag{23}$$

$$TQ_{cl2} = \begin{cases} \tau_{cl}\Omega_r & \left|\Omega_r\right| < \varepsilon \\ p_{cl2}\mu_{cl}\, 2\pi\, R_{cl2}^{\;2} L_{cl2} \operatorname{sgn}(\Omega_r) & \left|\Omega_r\right| \geq \varepsilon \end{cases} \tag{24}$$

Here, Ω_{cg1} and Ω_{cg2} are the upstream and downstream clutch disk rotation speeds of clutch no. 1 and Ω_r is the ring gear rotation speed at clutch no. 2. Here μ_{cl} and τ_{cl} are clutch friction and viscous torque coefficients (Ref. 16). Also, in clutch no. 1 (disk-type clutch) the torque is a function of the disk radius R_{cl1}, while for clutch no. 2 (cylindrical clutch) the torque is depends on clutch radius, R_{cl2}, and axial length L_{cl2}.

In each case, the clutch torque transitions from a viscous mode to a Coulomb friction mode based on a clutch slip velocity threshold parameter ε. Here, when clutch slip speed exceeds ε, the torque transitions from a viscous mode into the slipping mode (Coulomb friction). By proper selection of ε and τ_{cl}, the viscous mode numerically approximates clutch lockup without no need for explicit model DOF reduction (Ref. 6). The DCT system parameters used in this investigation are summarized in Table 2.

TABLE 2.—DCT PARAMETERS.

Parameter	Value
Number of gear teeth	Z_i=40, Z_{cg1}=42, Z_{cg2}=29, Z_{cg3}=52, Z_r=74, Z_p=14, Z_s=46
Gear radii, m	R_i=0.1, R_{cg1}=0.106, R_{cg2}=0.074, R_{cg3}=0.132, R_r=0.19, R_p=0.036, R_s=0.12, R_{cr}=0.152
Rotational inertias, kg m^2	J_i=0.064, J_{cg1}=0.078, J_{cg2}=0.039, J_{cg3}=0.402, J_r=1.766, J_p=0.002, J_s=0.264, J_{cr}=0.848
Number of planets	$N_p = 8$
Planet mass, kg	$m_p = 3.576$
Planet clutch radius (clutch 1), m	$R_{cl1} = 0.238$
Number of planet clutches (clutch 1)	$N_{cg} = 2$
Ring clutch dimensions (clutch 2), m	$R_{cl2} = 0.197$, $L_{cl2} = 0.1$
Clutch friction coefficient	$\mu_{cl} = 0.45$

Forward Flight Rotor (Propeller) Model

To include the rotor torque and resulting thrust for the tiltrotor in forward flight airplane mode with vehicle speed v_c, a rigid propeller model based on a standard blade element theory approach with quasi-steady aerodynamics (Ref. 10) is utilized (see Fig. 11). Here the differential rotor thrust dFT_{MR} and torque dTQ_{MR} at blade radial location r are expressed as

$$\begin{aligned} dFT_{MR} &= N_b(dL\cos\phi - dD\sin\phi) \\ dTQ_{MR} &= N_b r(dL\sin\phi + dD\cos\phi) \end{aligned} \tag{25}$$

Where dL and dD are differential blade lift and drag force increments along with the number of blades N_b.

Based on tangential blade speed, $u_T = \Omega_{MR}r$, together with v_c and the induced inflow velocity v_{ind}, the total inflow angle ϕ is

$$\phi = \phi_c + \phi_{ind} \tag{26-a}$$

With

$$\phi_c = \tan^{-1}\left[\frac{v_c}{\Omega_{MR}r}\right] \text{ and } \phi_{ind} = \frac{v_{ind}}{\sqrt{v_c^{\;2} + \Omega_{MR}^{\;2} r^2}} \tag{26-b}$$

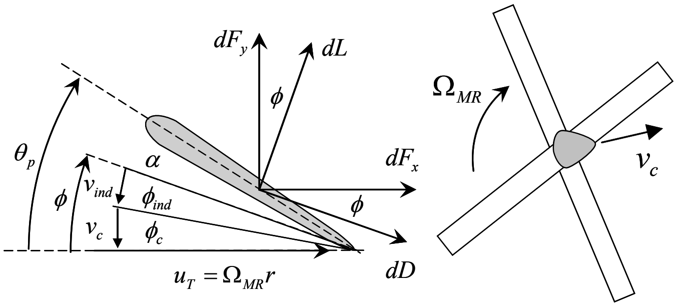

Figure 11.—Propeller in forward flight.

Where the induced inflow angle, ϕ_{ind}, is assumed small. Now, assuming uniform induced inflow velocity v_{ind} together with uniform blade pitch, θ_p, the following expression for total rotor thrust is obtained as

$$FT_{MR} = \frac{\rho_{air} a_{cL} c N_b \Omega_{MR}}{2} \int_0^{Rb} \Psi_c (\phi_c + \phi_{ind} - \theta_p) (v_c \phi_{ind} - r\Omega_{MR}) r dr \tag{27}$$

Similarly the corresponding rotor torque is

$$TQ_{MR} = \frac{\rho_{air} c_D c N_b \Omega_{MR}}{2} \int_0^{Rb} \Psi_c \left(r\Omega_{MR} - v_c \phi_{ind} \right) r^2 dr \ \ldots - \frac{\rho_{air} a_{cL} c N_b \Omega_{MR}}{2} \int_0^{Rb} \Psi_c \left(\phi_c + \phi_{ind} - \theta_p \right) \left(v_c + r\Omega_{MR} \phi_{ind} \right) r^2 dr \tag{28}$$

Both with

$$\Psi_c = \sqrt{1 + \frac{{v_c}^2}{r^2 {\Omega_{MR}}^2}} \tag{29}$$

With air density ρ_{air}, rotor radius, R_b and blade chord c. Also c_D is the blade section drag coefficient and a_{cL} is blade section lift coefficient slope.

Next, by equating the thrust expression in (27) with an expression based on momentum theory (Ref. 10), we obtain the following equation for the induced inflow ratio λ_{ind}

$$a_\lambda {\lambda_{ind}}^2 + b_\lambda \lambda_{ind} + c_\lambda = 0 \tag{30-a}$$

with coefficients

$$a_\lambda = 48 \ln\left[\frac{\gamma_c}{\lambda_c}\right] {\lambda_c}^2 + 6 a_{cL} \sigma \ln\left[\frac{1+\gamma_c}{\lambda_c}\right] \lambda_c - 24 \tag{30-b}$$

$$b_\lambda = 24 \sin^{-1}\left[\frac{1}{\lambda_c}\right] {\lambda_c}^3 + 6 a_{cL} \sigma \ln\left[\frac{\gamma_c}{\lambda_c}\right] {\lambda_c}^2 + \ldots \left(-24\gamma_c + 6 a_{cL} \sigma \tan^{-1} \lambda_c - 6 a_{cL} \sigma \theta_p \right) \lambda_c - 3 a_{cL} \sigma \tag{30-c}$$

$$c_\lambda = a_{cL} \sigma \left(\pi - 2\theta_p - \ln\left[\frac{1+\gamma_c}{\lambda_c}\right] \right) {\lambda_c}^3 \ldots - 2 a_{cL} \gamma_c \sigma \tan^{-1}[\lambda_c] {\lambda_c}^2 \ldots - a_{cL} \gamma_c \sigma \lambda_c + 2 a_{cL} \gamma_c \sigma \left({\gamma_c}^2 \theta_p - \tan^{-1} \lambda_c \right) \tag{30-d}$$

With induced and forward speed inflow ratios

$$\lambda_{ind} = \frac{v_{ind}}{R_b \Omega_{MR}}, \ \lambda_c = \frac{v_c}{R_b \Omega_{MR}} \ \text{and} \ \gamma_c = \sqrt{1 + {\lambda_c}^2} \tag{31}$$

and rotor solidity ratio

$$\sigma = \frac{c N_b}{\pi R_b} \tag{32}$$

Based on (30)-(32), the induced velocity, v_{ind}, is determined from the roots of (30-a). Using this result in (27)-(28), the rotor thrust and torque values can be computed for a given rotor speed, forward speed and blade pitch angle as shown in the rotor thrust and torque simulation block in Figure 12.

Using (1)-(3) and (21), the main rotor speed in high and low ratio are

$$\begin{aligned} \Omega_{MR,\text{high}} &= n_f n_{DCT,\text{high}} n_i \Omega_{pt} \\ \Omega_{MR,\text{low}} &= n_f n_{DCT,\text{low}} n_i \Omega_{pt} \end{aligned} \tag{33}$$

The rotor parameters used in this investigation are summarized in Table 3.

TABLE 3.—ROTOR PARAMETERS

Parameter	Value
Rotor speed (high), $\Omega_{MR,\text{high}}$	190 RPM
Rotor speed (low), $\Omega_{MR,\text{low}}$	102.5 RPM
Number of blades, N_b	4
Rotor radius, R_b	9.91 m
Rotor solidity, σ	0.13
Blade mass, m_b	372 kg
Rotor rotational inertia, J_{MR}	4.874×10^4 kg m^2
Section lift coefficient, c_D	0.012
Section drag coefficient, a_{Cl}	5.056

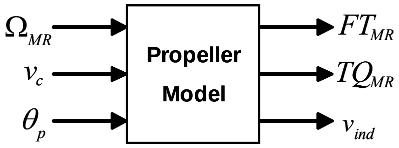

Figure 12.—Rotor thrust and torque simulation block.

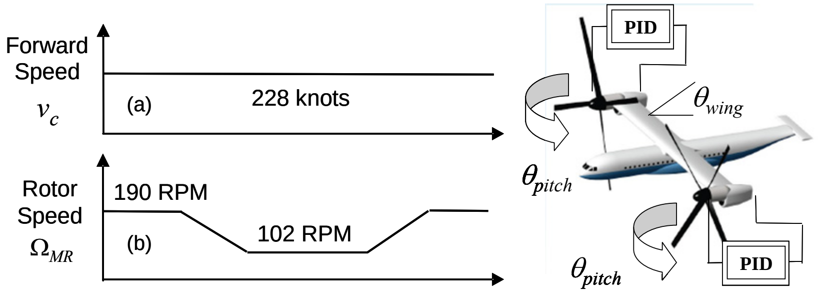

Figure 13.—Mission scenario; downshift and upshift in steady forward cruise using SSC shifting.

Two-Speed Shift Simulation Results

Utilizing the model summarized in the previous section, this portion of the paper presents a two-speed shift simulation case study for the tiltrotor DCT drive-system (Fig. 2) operating in airplane mode at an intermediate steady forward cruising speed. The operating conditions and parameters used in the simulation (see Tables 1 to 3) are based on the LCTR-2 (Refs. 12 and 18). Specifically, the simulated mission scenario, depicted in Figure 13, is a rotor speed downshift followed later by a rotor speed upshift both while operating at the constant forward speed setpoint, $v_{c,\text{set}} = 228$ knots.

To avoid shifting under full power, the SSC strategy, presented in (Ref. 9), is utilized in both downshift and upshift phases. Fundamentally, the SSC method utilizes the freewheel clutches at the power turbine output to disengage each engine sequentially wherein shifting along the particular driveline path can be performed in an unloaded condition. Since the FWU prevents the power turbine from being driven by the load, it will disengage when the load speed becomes larger that of the power turbine. In a multi-engine driveline equipped with a variable ratio gearbox there are essentially two situations which can cause a specific FWU to disengage; 1) by lowering the power turbine setpoint speed of that engine or, 2) by downshifting the gearbox in that engine’s driveline path. In the first situation, the remaining engines maintain the system speeds as the particular engine speed is lowered. In second the situation, the commanded downshift acts as an upshift on the gearbox input side thus increasing the load speed at the FWU. Since the engine setpoint speed remains fixed, the FWU in this driveline path will disengage. Both of these situations arise in the SSC shifting method. The downshift and upshift portions of this simulation are presented separately in the following two subsections. Here the effects of shift rate on the engine response will be explored in detail.

Forward Cruise SSC Downshift

The timeline of the SSC downshift procedure along with a brief description of each event is given in Table 4.

TABLE 4.—SSC DOWNSHIFT TIMELINE*

Time	Commands	Comments
t=12 sec	1) Disable engine torque sharing control loop 2) Start left side DCT downshift (disengage clutch no. 1 and engage clutch no. 2). $\dot{p}_{cl1} = -30$ psi/sec $\dot{p}_{cl2} = +4$ psi/sec	Start of SSC downshift procedure Increases left DCT input shaft speed which disengages left engine FWU
t=32 sec	3) Start right engine power turbine setpoint ramp-down (-600 RPM/sec)	Main rotor speed reduces from 190 to 102.5 RPM Left engine re-engages FWU at end of ramp-down
t=52 sec	4) Start right side DCT downshift (disengage clutch no. 1 and engage clutch no. 2). $\dot{p}_{cl1} = -30$ psi/sec $\dot{p}_{cl2} = +4$ psi/sec	Increases right DCT input shaft speed which disengages right engine FWU
t=72 sec	5) Start right engine power turbine setpoint ramp-up (+600 RPM/sec)	Right engine re-engages FWU at end of ramp-up
t=82 sec	6) Re-enable engine torque sharing control loop	End of SSC downshift procedure

*Under constant forward speed setpoint $v_{c,set} = 228$ knots.

Figures 14 to 19 give the forward cruise SSC downshift response of the two-speed DCT tiltrotor system. By examining Figures 14(a) and (b), it is apparent that the rotor speed is successfully lowered with very little deviation in forward velocity. Also note in Figure 14(b) that the left and right rotor speeds are nearly identical throughout the shift. Figures 14(c) and (d) show the open-loop DCT clutch pressure command inputs used to sequentially downshift the left and right side DCTs (step nos. 2 and 4 in Table 4). Furthermore, the engine power turbine speeds are shown in Figure 14(e) and (f). In Figure 14(e) it is observed that, even though the left side engine setpoint speed remains constant, the power turbine transiently increases due to the left side DCT downshift. This is a result of the rapid unloading due to FWU disengagement (see step no. 2 in Table 4). According to step nos. 3 and 5 in Table 4, Figure 14(f) shows the ramp-down and ramp-up of the right engine power turbine. Similarly, when the right side DCT is downshifted, the right engine power turbine experiences a transient speed increase above its setpoint as its FWU disengages (see step no. 4 in Table 4).

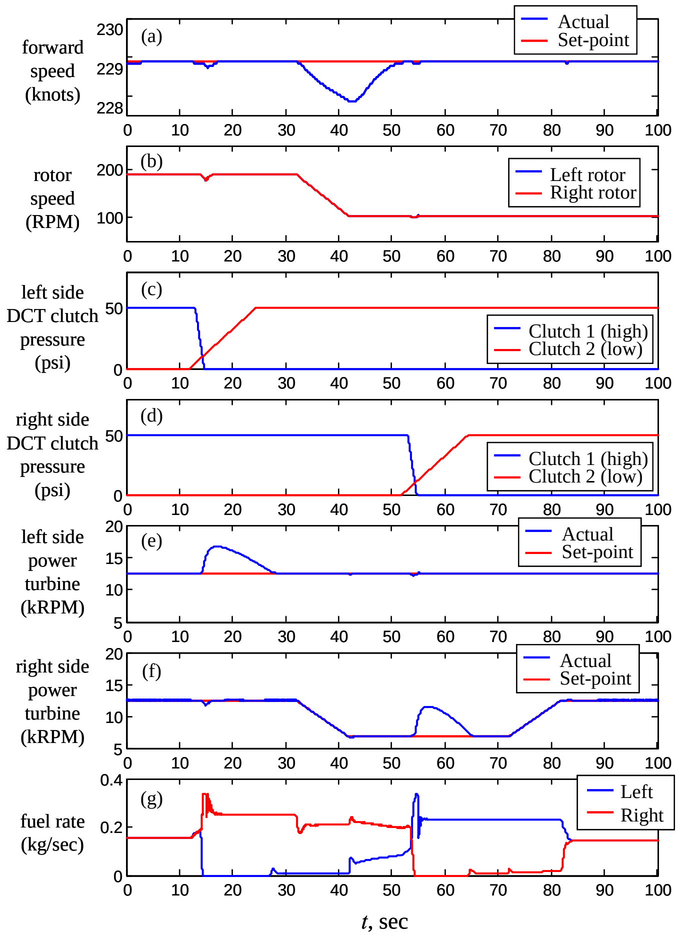

Figure 14.—Forward cruise SSC downshift simulation; (a) forward speed, (b) rotor speed, (c) left DCT shift commands, (d) right DCT shift commands, (e) left power turbine speed, (f) right power turbine speed (g) fuel rates.

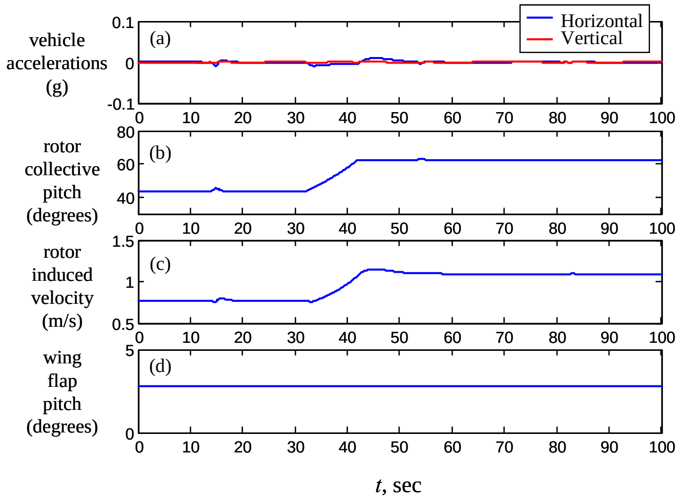

Figure 15.—Forward cruise SSC downshift—flight dynamics; (a) vehicle acceleration, (b) collective pitch, (c) induced velocity, (d) wing flap angle.

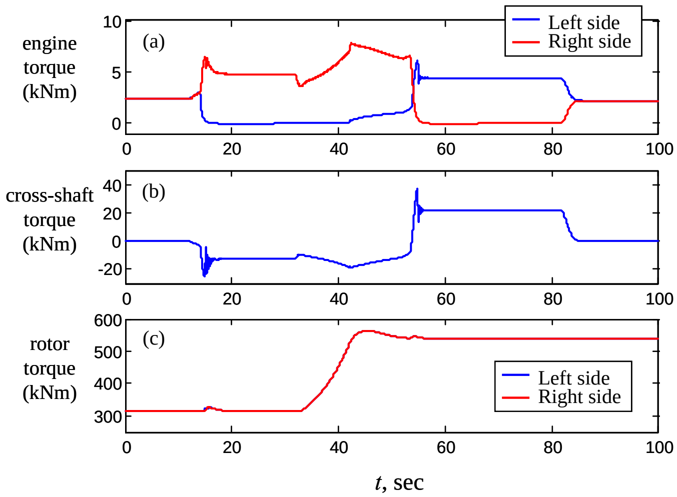

Figure 16.—Forward cruise SSC downshift—torque response; (a) engine torques, (b) cross-shaft torque, (c) rotor torque.

Figure 14(g) shows the corresponding fuel rates commanded by the closed-loop engine fuel control for both the left and right side engines. Note, the left and right side engine fuel rates are equivalent prior to disabling (*t*=12 sec) and after re-enabling (*t*=82 sec) the multi-engine torque sharing control loop (see step nos. 1 and 6 in Table 4).

The flight dynamics are summarized in Figure 15. Figure 15(a) shows that both the horizontal and vertical vehicle accelerations are minimal. Thus, no forward speed or altitude is lost during the downshift. In order to maintain the constant forward speed setpoint under the decreasing rotor speed, the closed-loop blade pitch controller increases the blade collective pitch to keep constant thrust as shown Figure 15(b). This results in a corresponding increase in rotor induced velocity is seen in Figure 15(c). Finally, as seen in Figure 15(d), under this constant thrust condition, there is no appreciable change in wing flap angle.

The driveline torques are summarized in Figure 16. As observed in the engine fuel rate response in Figure 14 (g), the left and right side power turbine torques are identical prior to *t*=12 sec and after *t*=82 sec. During the downshift, the engine torques become dissimilar and are due to both rotor aerodynamic torque as well as acceleration torque demands.

As a result of the dissimilar left and right engine torques, the cross-shaft also becomes loaded as shown in Figure 16(b). Finally, Figure 16(c) shows the increasing rotor torque which is a result from the increasing collective pitch and constant thrust requirement (see Fig. 15(b)). Note that the left and right rotor torques are identical throughout the shift (Fig. 16(c)).

Other important aspects of the two-spool gas turbine engine response are shown in Figures 17 and 18. In particular, by plotting compressor pressure ratio versus air mass flow, the left and right engine transient operating lines during the SSC downshift are shown in Figure 18.

Figure 18 shows that both engines experience a wide range of operation during the SSC process and that both engines transiently pass over the surge line. Since Figure 18 does not show temporal information, the engine surge margin (SM) versus time is examined. Here, the working definition of SM used is

$$SM = \frac{pr_{c,\text{surge}} - pr_c}{pr_{c,\text{surge}}} \times 100\% \qquad (34)$$

Therefore SM > 0 indicates no compressor surging. In this analysis, three different DCT shift rate cases (slow, medium and fast) as given in Table 5 are considered. Note the medium case corresponds to the values used thus far in Figures 14 to 18.

TABLE 5.—DCT DOWNSHIFT RATE CASES

Case	DCT clutch pressure engagement and disengagement rates (psi/sec)	
Slow	Clutch no. 1 disengagement rate, $\dot{p}_{cl1} = -15$ psi/sec	Clutch no. 2 engagement rate, $\dot{p}_{cl2} = 4$ psi/sec
Medium	Clutch no. 1 disengagement rate, $\dot{p}_{cl1} = -30$ psi/sec	Clutch no. 2 engagement rate, $\dot{p}_{cl2} = 4$ psi/sec
Fast	Clutch no. 1 disengagement rate, $\dot{p}_{cl1} = -300$ psi/sec	Clutch no. 2 engagement rate, $\dot{p}_{cl2} = 4$ psi/sec

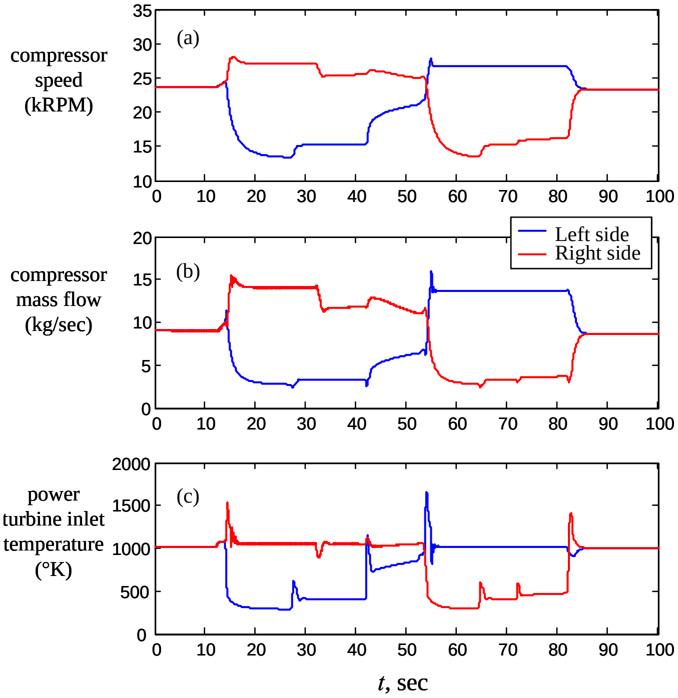

Figure 17.—Forward cruise SSC downshift—engine response; (a) compressor speed, (b) mass flow, (c) power turbine inlet temperature.

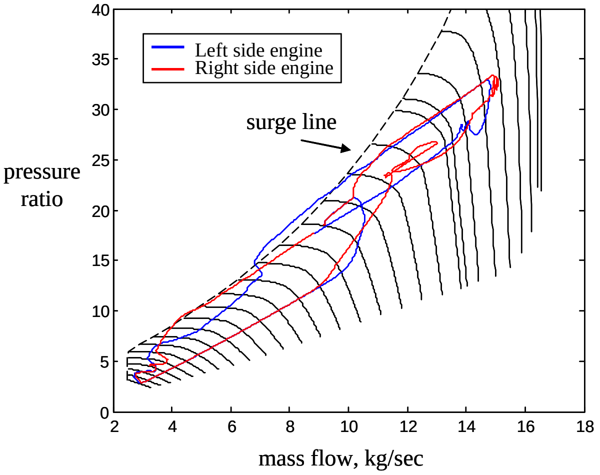

Figure 18.—Forward cruise SSC downshift—two-spool gas turbine engine transient running lines.

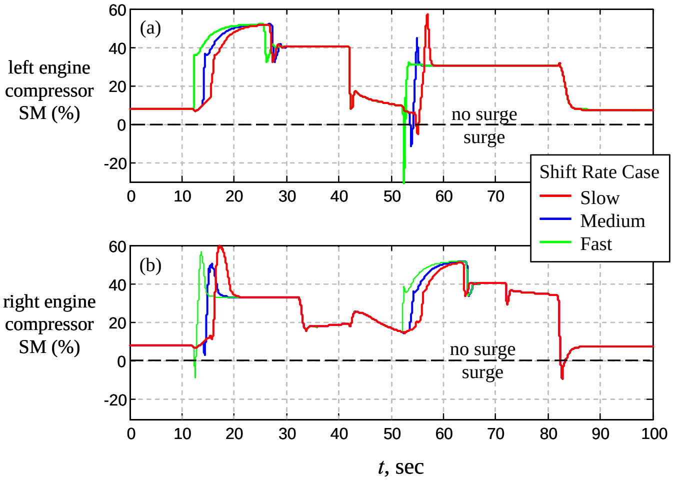

Figure 19.—Forward cruise SSC downshift—engine compressor surge margins for three DCT shift rates.

The resulting SM values for the left and right engines are shown in Figures 19(a) and (b). In each case, the surge line is crossed very briefly. Here, Figure 19(a) shows that the left engine crosses the SM immediately after *t*= 52 sec as the right DCT begins to downshift (step no. 4, Table 4). Thus, the left engine surge is a result of the transient shock due to the unloading the right engine FWU.

Furthermore, Figure 19(b) shows that the right engine experiences a brief surge near the start and end of the downshift process for similar reasons as the left engine. Specifically, the first surge of the right engine is due to the initial disengagement of the left engine FWU (step no. 1, Table 4) and the second surge occurs when the left engine re-engages the FWU at the end of its ramp-up (step no. 5, Table 4). Figure 19 shows that slower DCT shifting rates are more beneficial for the engine surge margins in the SSC downshift procedure.

Forward Cruise SSC Upshift

Next, the simulation results of the SSC upshift procedure, which is essentially the process reverse of the SSC downshift, are described. The SSC upshift timeline is given in Table 6.

TABLE 6.—SSC UPSHIFT TIMELINE*

Time	Commands	Comments
t=7 sec	1) Disable engine torque sharing control loop 2) Start right engine power turbine setpoint ramp-down (–600 RPM/sec)	Start of SSC upshift procedure Disengages right engine FWU
t=27 sec	3) Start right side DCT upshift (disengage clutch no. 2 and engage clutch no. 1). $\dot{p}_{cl1} = +4$ psi/sec $\dot{p}_{cl2} = -30$ psi/sec	Decreases right DCT input shaft speed. Right engine FWU becomes re-engaged
t=47 sec	4) Start right engine power turbine setpoint ramp-up (+230 RPM/sec)	Main rotor speed increases from 102.5 to 190 RPM Speed increase disengages left engine FWU
t=82 sec	5) Start left side DCT upshift (disengage clutch no. 2 and engage clutch no. 1). $\dot{p}_{cl1} = +4$ psi/sec $\dot{p}_{cl2} = -30$ psi/sec	Decreases left DCT input shaft speed which re-engages left engine FWU
t=92 sec	6) Re-enable engine torque sharing control loop	End of SSC upshift procedure

*Under constant forward speed setpoint $v_{c,\text{set}}$ = 228 knots.

Figures 20 to 25 show the forward cruise SSC upshift response of the two-speed DCT tiltrotor. By examining the forward speed and the rotor speed in Figures 20(a) and(b), it is apparent that rotor speed is successfully increased with little deviation in forward velocity. Figures 20(c) and (d) show the open-loop DCT clutch pressure command inputs used to sequentially upshift the right and left side DCTs (step nos. 3 and 5 in Table 6). Furthermore, the engine power turbine speeds are shown in Figure 20(e) and (f). In Figure 20(e) it is observed that the left power turbine speed transiently increases due to the right engine ramp-up. This is due to the unloading of the left engine FWU. (See step no. 4 in Table 6). According to step nos. 2 and 4 in Table 6, Figure 20(f) shows the ramp-down and ramp-up of the right engine power turbine. Figure 20(g) shows the corresponding fuel rates commanded by the closed-loop engine fuel control for both the left and right engines. Note, the left and right side engine fuel rates are equivalent prior to disabling (*t*=7 sec) and after re-enabling (*t*=92 sec) the multi-engine torque sharing control loop (see step nos. 1 and 6 in Table 6).

Also note that the fuel rate is essentially flat during the rotor speed acceleration phase (step no. 4, Table 6). This is due to the fact that as rotor speed increases, the collective pitch is automatically decreased by the forward speed pitch controller to maintain constant thrust as further shown in Figure 21.

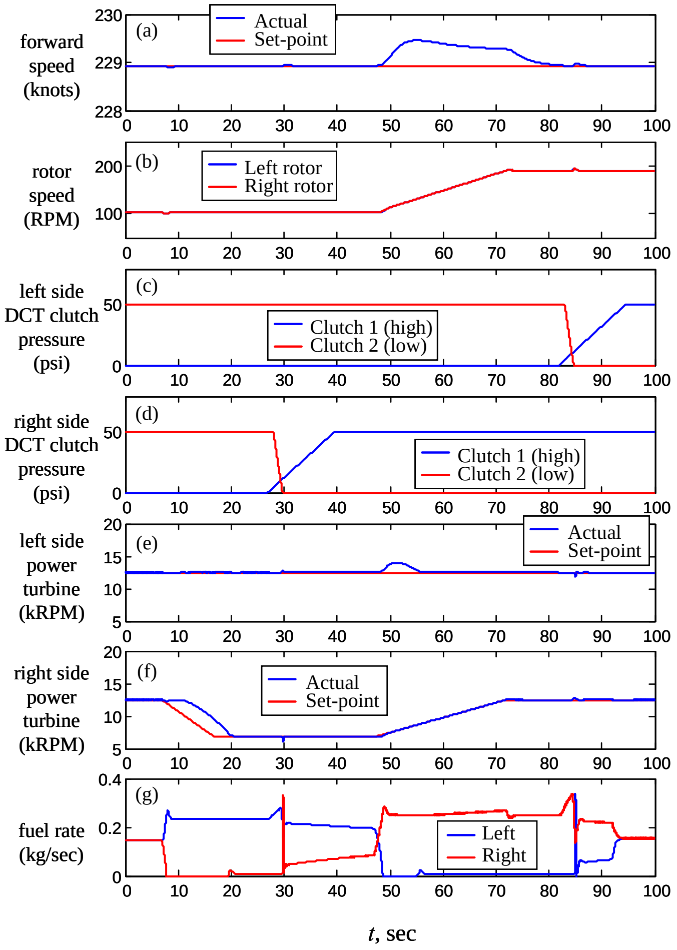

Figure 20.—Forward cruise SSC upshift simulation; (a) forward speed, (b) rotor speed, (c) left DCT shift commands, (d) right DCT shift commands, (e) left power turbine speed, (f) right power turbine speed (g) fuel rates.

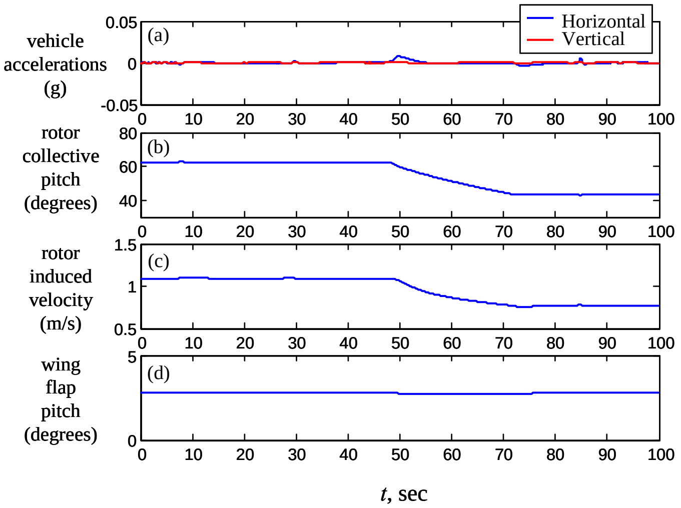

Figure 21.—Forward cruise SSC upshift—light dynamics; (a) vehicle acceleration, (b) collective pitch, (c) induced velocity, (d) wing flap angle.

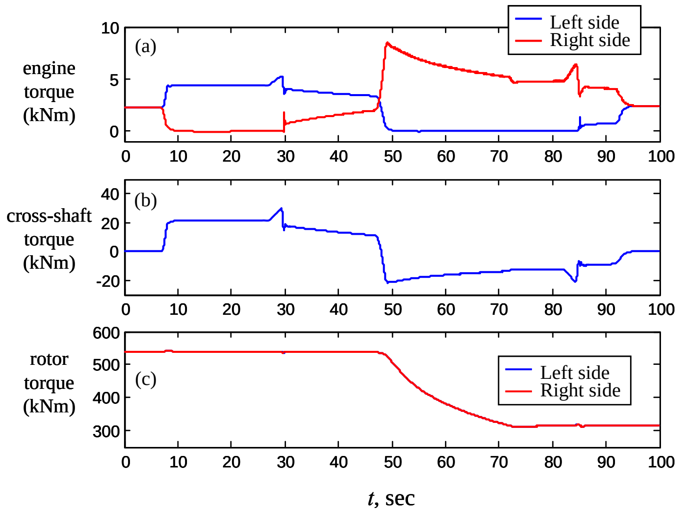

Figure 22.—Forward cruise SSC upshift—torque response; (a) engine torques, (b) cross-shaft torque, (c) rotor torque.

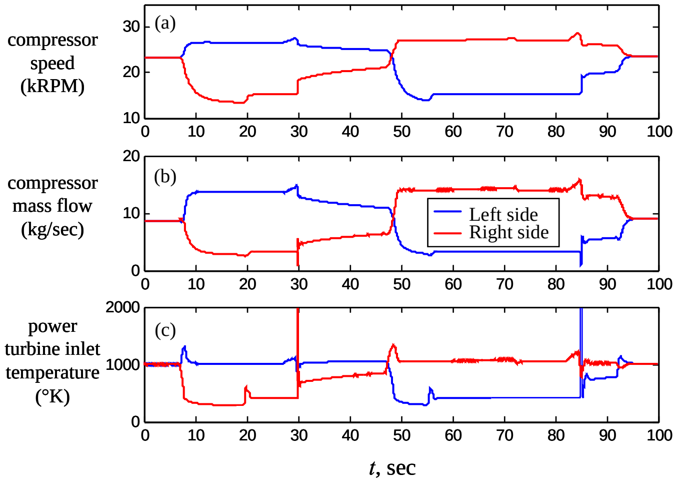

Figure 23.—Forward cruise SSC upshift—engine response; (a) compressor speed, (b) mass flow, (c) power turbine inlet temperature.

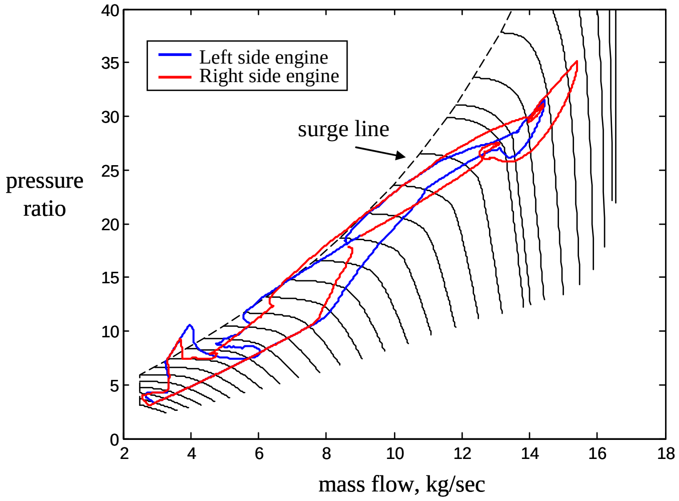

Figure 24.—Forward cruise SSC upshift—two-spool gas turbine engine transient running lines.

Similar to the downshift case, Figure 21(a) shows that both the horizontal and vertical vehicle accelerations are minimal thus with no forward speed or altitude lost during the upshift. To maintain constant forward speed under the increasing rotor speed, the closed-loop blade pitch controller decreases the blade collective pitch to keep constant thrust as shown Figure 21(b). This causes the drop in induced velocity as seen in Figure 21(c). Finally, as seen in Figure 21(d), under the constant thrust condition, there is no appreciable change in wing flap angle.

The driveline torques are summarized in Figure 22. As observed in the engine fuel rate response in Figure 20(g), the left and right side power turbine torques are identical prior to t=7 sec and after t=92 sec. During the downshift, the engine torques become dissimilar and are due to both rotor aerodynamic torque as well as acceleration torque demand.

As a result of the dissimilar left and right engine torques, the cross-shaft also becomes loaded as shown in Figure 22(b). Here, the cross-shaft is subjected to a fully reversing torque load. This is also true in the downshift case. Finally, Figure 22(c) shows the deceasing rotor torque which is a result from the decreasing collective pitch.

Other important aspects of the two-spool gas turbine engine response are shown in Figures 23 and 24. As seen in Figure 24, similar to the downshift case, the transient running lines of each engine undergo small excursions past the compressor surge line during the SSC upshift process.

Next, as in the downshift case, three different DCT shift rates (slow, medium and fast), given by Table 7, are examined. Note the medium case corresponds to the values used in Figures 20 to 24.

TABLE 7.—UPSHIFT RATE CASES

Case	DCT clutch pressure engagement and disengagement rates (psi/sec)	
Slow	Clutch no. 1 engagement rate, $\dot{p}_{cl1} = 4$ psi/sec	Clutch no. 2 disengagement rate, $\dot{p}_{cl2} = -15$ psi/sec
Medium	Clutch no. 1 engagement rate, $\dot{p}_{cl1} = 4$ psi/sec	Clutch no. 2 disengagement rate, $\dot{p}_{cl2} = -30$ psi/sec
Fast	Clutch no. 1 engagement rate, $\dot{p}_{cl1} = 4$ psi/sec	Clutch no. 2 disengagement rate, $\dot{p}_{cl2} = -300$ psi/sec

The resulting SM values for each shift rate are shown in Figure 25. In each case, the surge line is crossed briefly. Figure 25(a) shows that the left engine crosses the surge line when the FWU re-engages due to the left side DCT upshift (step no. 5, Table 6). Furthermore the right engine experiences a surge near $t = 30$ sec and $t = 48$ sec. The first surge of the right engine is due to re-engagement of the right engine FWU as a result of the right side DCT upshift (step no. 3, Table 6). The second surge, near $t = 48$ sec, is due to the right engine power turbine set-point ramp-up (step no. 4, Table 6) which causes the left engine to disengage from its FWU.

Finally, Figure 25 shows that faster DCT shifting rates are more beneficial for the engine surge margins in the SSC upshift procedure.

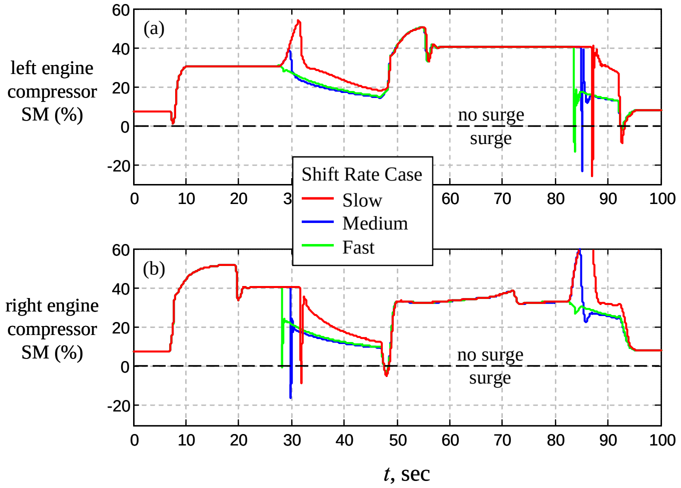

Figure 25.—Forward cruise SSC upshift—engine compressor surge margins for three DCT shift rates.

Conclusions

This investigation explores the variable-speed operation and transient shift response of a prototypical two-speed dual-clutch transmission tiltrotor driveline based on the NASA LCTR-2 in forward flight airplane mode. A comprehensive variable-speed rotorcraft propulsion system modeling tool developed under a NASA-funded NRA program is utilized to simulate the drive system dynamics. In this study, a sequential shifting control strategy is analyzed under a steady cruise condition. This investigation attempts to build upon previous variable-speed rotorcraft propulsion studies by 1) including a fully nonlinear transient gas-turbine engine model, 2) including clutch stick-slip friction effects, 3) including shaft flexibility, and 4), incorporating a basic flight dynamics model to account for interactions with the flight control system. Sequential shifting provided smooth rotor speed changes while maintaining a constant forward speed setpoint and a constant altitude for the tiltrotor studied. However, it was also found that transient shocks produced by engine engagements and disengagements from their freewheeling clutches tended to produce brief excursions of the engine compressor surge limit. It was found that proper choice of dual-clutch transmission shift rate could minimize these excursions. In the sequential downshift case, it was found that slower shift rates tended to reduce the engine surge effects while the opposite trend was found for the upshift case. Through exploring these interactions between the various subsystems, this analysis provides important insights into the continuing development of variable-speed rotorcraft propulsion technology.

References

1. Johnson, W., Yamauchi G.K., and Watts M.E., “NASA Heavy Lift Rotorcraft Systems Investigation.” NASA 213467, December 2005.
2. Goi, T., Kawakami, K., Yamakawa, E., and Tanaka, H., “Variable Rotor Speed Transmission with High Speed Traction Drive,” American Helicopter Society 55th Annual Forum, Montreal, Quebec, Canada, May 25-27, 1999.
3. Kish, J., “Vertical Lift Drive System Concept Studies Variable Speed/Two-Speed Transmissions,” NASA/CR—2002-211564, 2002.
4. Acree, C.W., Yeo, H., and Sinsay, J.D., “Performance Optimization of the NASA Large Civil Tiltrotor,” International Powered Lift Conference, London, UK, Jul. 22-24, 2008.
5. Stevens, M.A, Handschuh, R.F., and Lewicki, D.G., “Concepts for Variable/Multi-Speed Rotorcraft Drive System,” AHS 64th Annual Forum and Technology Display, Montreal Canada, April 29–May 1, 2008
6. Lewicki, D.G., DeSmidt H., Smith, E.C., and Bauman, S.W., “Dynamics of a Dual Clutch Gearbox System: Analysis and Experimental Validation,” AHS 66th Annual Forum and Technology Display, Phoenix, AZ, May 11-13, 2010.
7. Kulkarni, M., Shim, T., and Zhang, Y., “Shift Dynamics and Control of Dual-Clutch Transmissions”, Mechanisms and Machine Theory, 42, pp. 168-182, (2007).
8. Lui, C.H., “Simulation Study of Dual Clutch Transmission for Medium-Duty Truck Applications,” SAE, 2005-01-3590 (2005).
9. Litt, J.S., Edwards, J.M., and DeCastro, J.A., “A Sequential Shifting Algorithm for Variable Rotor Speed Control,” NASA/TM—2007-214842 (2007).
10. Johnson, W., Helicopter Theory, University Press, Princeton, NJ, 1980.
11. Walsh, P. P., and Fletcher, P., Gas Turbine Performance, Wiley-Blackwell; 2nd Edition, Oxford, 2004.
12. Veres, J. P., 2009, “Compressor Study to Meet Large Civil Tilt Rotor Engine Requirements,” AHS International, 65th Annual Forum & Technology Display, Grapevine, TX, May 27–29, 2009.
13. Snyder, C.A., and Thurman, D.R., “Gas turbine characteristics for a Large Civil Tilt-Rotor (LCTR),” AHS International, 65th Annual Forum & Technology Display, Grapevine, TX, May 27–29, 2009.
14. Camporeale, S.M., Fortunato, B., and Mastrovito, M. “A Modular Code for Real Time Dynamics Simulation of Gas Turbines in Simulink,” Trans. ASME: J. Eng. Gas Turbines Power, 128, pp. 506-517, (2006).
15. Sekhon, R., Bassily, H., Wagner, J., and Gaddis, J.. 2006, “Stationary Gas Turbines – A Real Time Dynamic Model with Experimental Validation,” Proc. of the 2006 American Control Conference, Minneapolis, MN, June 14-16, 2006.
16. Crowther, A., Zhang, N., Liu, D.K., Jeyakumaran, J.K., “Analysis and Simulation of Clutch Engagement Judder and Stick-Slip in Automotive Powertrain Systems, Proc. Instn Mech. Engrs, Part D: J. Automobile Engineering, 218, pp. 1427-1446, (2004).
17. Liu, Y., Qin, D., Jiang, H. and Zhang, Y., “A Systematic Model for Dynamics and Control of Dual Clutch Transmissions,” Journal of Mechanical Design, ASME Trans. 131 (2009) 061012.
18. Acree, C.W. and Johnson, W., “Aeroelastic Stability of the LCTR-2 Civil Tiltrotor,” Presented at the AHS Technical Specialists’ Meeting, Dallas, TM, October 15-17, 2008.

Appendix A.—Nomenclature

A_i [i=1-7]	engine stage cross-section areas, m^2
a_{cL}	blade lift coefficient slope
a_λ, b_λ, c_λ	inflow ratio solution coefficients
C_a	compressor axial flow velocity, m/s
C_{an}	nominal compressor axial flow velocity, m/s
CVSRPM	comprehensive variable-speed rotorcraft propulsion system modeling
c	blade chord, m
c_D	blade drag coefficient
c_p	specific heat of air, kJ/(kg K)
DCT	dual-clutch transmission
DOF	degrees of freedom
dD	differential blade element drag, N
dF_x, dF_y	differential blade element force components, N
dL	differential blade element lift, N
f	fuel-air ratio
$\mathbf{F}$	DCT generalized force vector
FT_{MR}	main rotor thrust, N·m
FWU	freewheeling clutch units
ht_c	compressor inlet hub-to-tip ratio
ht_{pt}	power turbine inlet hub-to-tip ratio
J_c	compressor rotational inertia, kg m^2
J_{cgi} [i=1-3]	DCT control gear rotational inertias, kg m^2
J_{cr}	DCT carrier rotational inertia, kg m^2
J_{ggt}	gas generator turbine rotational inertia, kg m^2
J_i	DCT input gear rotational inertia, kg m^2
J_{in}	DCT input-side rotational inertia, kg m^2
$J_{out,}$	DCT output-side rotational inertia, kg m^2
J_p	DCT planet gear rotational inertia, kg m^2
J_{pt}	power turbine rotational inertia, kg m^2
J_r	DCT ring gear rotational inertia, kg m^2
J_s	DCT sun gear rotational inertia, kg m^2
L_{cl2}	ring gear clutch length, m
LHV	fuel lower heating value, J/kg
$\mathbf{M}$	DCT inertia matrix
m_b	blade mass, kg
m_p	DCT planet mass, kg
m_{pa}	plenum chamber air mass, kg
$\dot{m}_c$	compressor mass flow rate, kg/s
$\dot{m}_{cc}$	combustion chamber mass flow rate, kg/s
$\dot{m}_{cn}$	nominal compressor mass flow rate, kg/s
$\dot{m}_f$	fuel flow rate, kg/s
$\dot{m}_{f,\mathrm{max}}$	maximum fuel flow rate, kg/s
$\dot{m}_{fn}$	nominal fuel flow rate, kg/s
$\dot{m}_{ggt}$	gas generator mass flow rate, kg/s
$\dot{m}_{\mathrm{in}}$	plenum chamber input mass flow rate, kg/s
$\dot{m}_{\mathrm{out}}$	plenum chamber output mass flow rate, kg/s
$\dot{m}_{pt}$	power turbine mass flow rate, kg/s
N_b	number of main rotor blades
N_{cg}	number of DCT planet clutches
N_p	number of DCT planets
N_s	number of compressor stages
$n_{DCT,\mathrm{high}}$	DCT high speed ratio
$n_{DCT,\mathrm{low}}$	DCT low speed ratio
n_f	final gearbox ratio
n_i	initial reduction gearbox ratio
P_a	ambient pressure, bar
PGT	planetary gear transmission
PID	proportional-integral-derivative
p_{cli} [i=1-2]	clutch engagement pressures, N/m^2
$p_{cl\mathrm{max}}$	maximum clutch engagement pressure, N/m^2
P_p	plenum chamber pressure, N/m^2
P_{0i} [i=1-7]	engine stagnation pressures, N/m^2
pr_c	compressor pressure ratio
pr_{cn}	nominal compressor pressure ratio
$\mathbf{q}$	DCT degree-of-freedom vector
Q_{cc}	combustion chamber heat addition, W
r	blade element radial location, m
R	ideal gas constant, J/(mol K)
R_b	blade radius, m
R_c	compressor mean radius, m
R_{cgi} [i=1-3]	DCT control gear radii, m
R_{cli} [i=1-2]	clutch radii, m
R_{cr}	DCT carrier radius, m
R_i	DCT input gear radius, m
R_p	DCT planet gear radius, m
R_{pt}	power turbine mean radius, m
R_r	DCT ring gear radius, m
R_s	DCT sun gear radius, m
SM	compressor surge margin, percent
SSC	sequential shifting control
t	time, s
T_{0i} [i=1-7]	engine stage stagnation temperatures, K

T_a	ambient temperature, K
TQ_c	compressor torque, N·m
$TQ_{cl,i}$ [i=1-2]	clutch torques, N·m
TQ_{in}	DCT input shaft torque, N·m
TQ_{out}	DCT output shaft torque, N·m
u_T	blade element tangential speed, m/s
v_c	forward speed, knots
$v_{c,set}$	forward speed setpoint, knots
v_{ind}	induced velocity, knots
V_p	plenum chamber volume, m^3
W_c	compressor power, W
W_L	load power, W
W_{ggt}	gas generator turbine power, W
W_{pt}	power turbine power, W
x	vehicle horizontal position coordinate, m
y	vehicle vertical position coordinate, m
Z_{cgi} [i=1-3]	number of DCT control gear teeth
Z_i	number of DCT input gear teeth
Z_p	number of DCT planet gear teeth
Z_r	number of DCT ring gear teeth
Z_s	number of DCT sun gear teeth
α	angle of attack, rad
β_c	compressor beta parameter, s^2/kg^2
ΔT_{0cc}	combustion chamber temperature rise, K
ε	clutch slip velocity threshold, RPM
ϕ	total inflow angle, rad
ϕ_c	forward speed inflow angle, rad
ϕ_i	DCT input gear rotation, rad
ϕ_{ind}	induced inflow angle, rad
ϕ_r	DCT ring gear rotation, rad
γ	specific heat ratio
γ_c	forward speed inflow parameter
η_c	compressor isentropic efficiency
η_{cc}	combustion chamber loss coefficient
φ	choking mass flow parameter, $\text{s}/(\text{m}\sqrt{\text{K}})$
λ_c	forward speed inflow ratio
λ_{ind}	induced inflow ratio
μ_{cl}	clutch dry friction coefficient
θ_p	main rotor pitch angle, rad
θ_w	wing elevon flap angle, rad
ρ_{air}	ambient air density, kg/m^3
ρ_p	plenum chamber gas density, kg/m^3
σ	rotor solidity ratio
τ_{cc}	combustion chamber time constant, s
τ_{cl}	clutch viscous torque coefficient, kg m^2/s
Ψ_c	total speed ratio
Ω_c	compressor speed, RPM
Ω_{cn}	compressor nominal speed, RPM
Ω_{DCT}	two-speed transmission output speed, RPM
$\Omega_{DCT,\text{high}}$	two-speed transmission high output speed, RPM
$\Omega_{DCT,\text{in}}$	two-speed transmission input speed, RPM
$\Omega_{DCT,\text{low}}$	two-speed transmission low output speed, RPM
$\Omega_{FWU,\text{out}}$	freewheeling clutch output speed, RPM
$\Omega_{cg1,2}$	DCT planet clutch speeds, RPM
Ω_{MR}	main rotor speed, RPM
Ω_{pt}	power turbine speed, RPM
Ω_{ptn}	nominal power turbine speed, RPM
$\Omega_{pt,\text{set}}$	power turbine setpoint speed, RPM
Ω_r	DCT ring gear speed, RPM
$\dot{}$	Note, if not explicitly stated, a dot above a variable represents change with respect to time.

Appendix B.—Comprehensive Variable-Speed Rotorcraft Propulsion System Model

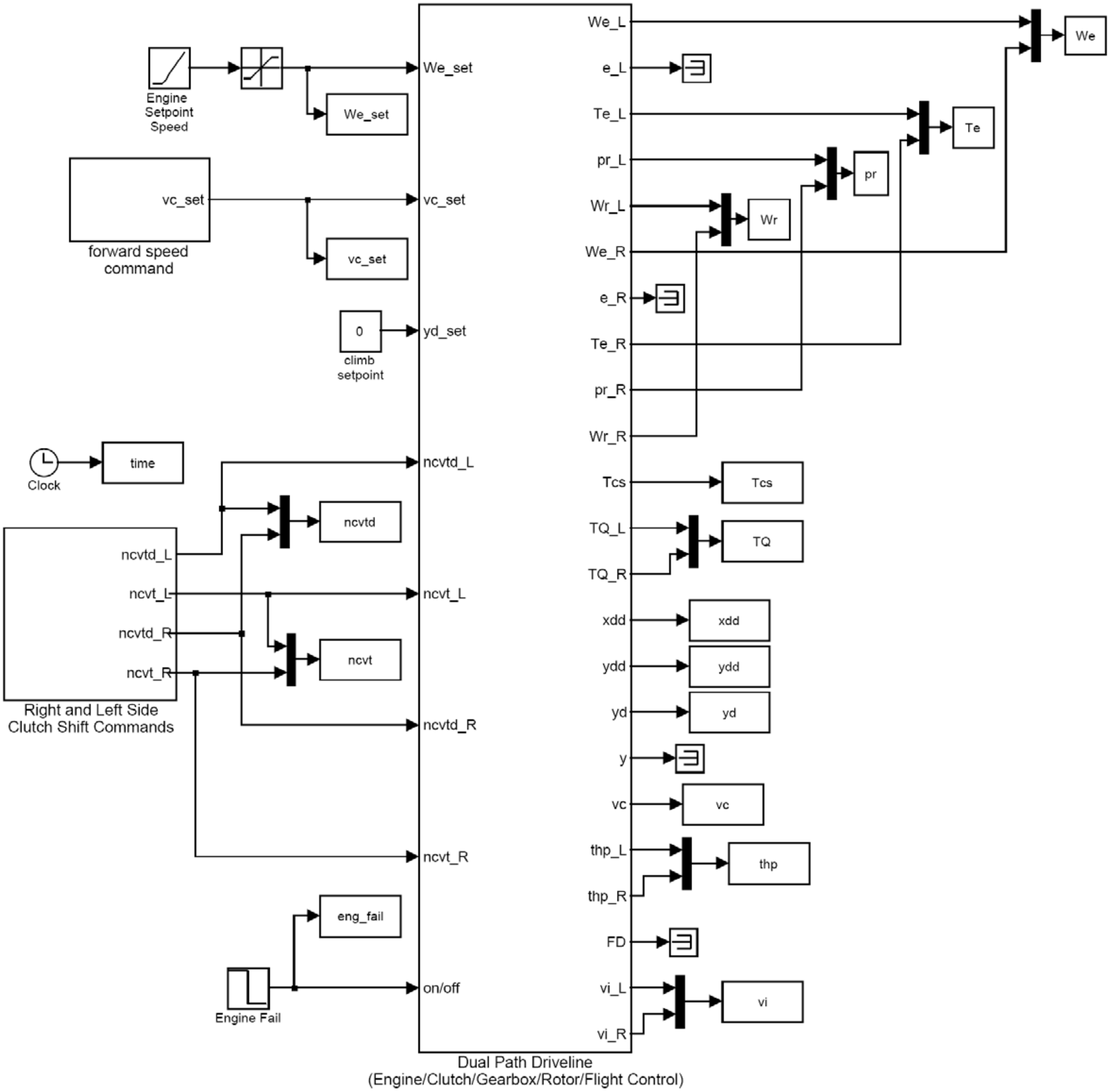
Engine Setpoint Speed
We_set
We_set
vc_set
forward speed command
vc_set
vc_set
0
climb setpoint
yd_set
Clock
time
ncvtd_L
ncvtd
Right and Left Side Clutch Shift Commands
ncvtd_L
ncvt_L
ncvtd_R
ncvt_R
ncvt_L
ncvt
ncvtd_R
ncvt_R
eng_fail
Engine Fail
on/off
Dual Path Driveline (Engine/Clutch/Gearbox/Rotor/Flight Control)
We_L
e_L
Te_L
pr_L
Wr_L
We_R
e_R
Te_R
pr_R
Wr_R
Tcs
TQ_L
TQ_R
xdd
ydd
yd
y
vc
thp_L
thp_R
FD
vi_L
vi_R
We
Te
pr
Wr
Tcs
TQ
xdd
ydd
yd
vc
thp
vi

Figure B-1.—Two-speed rotorcraft driveline comprehensive simulation—main block.

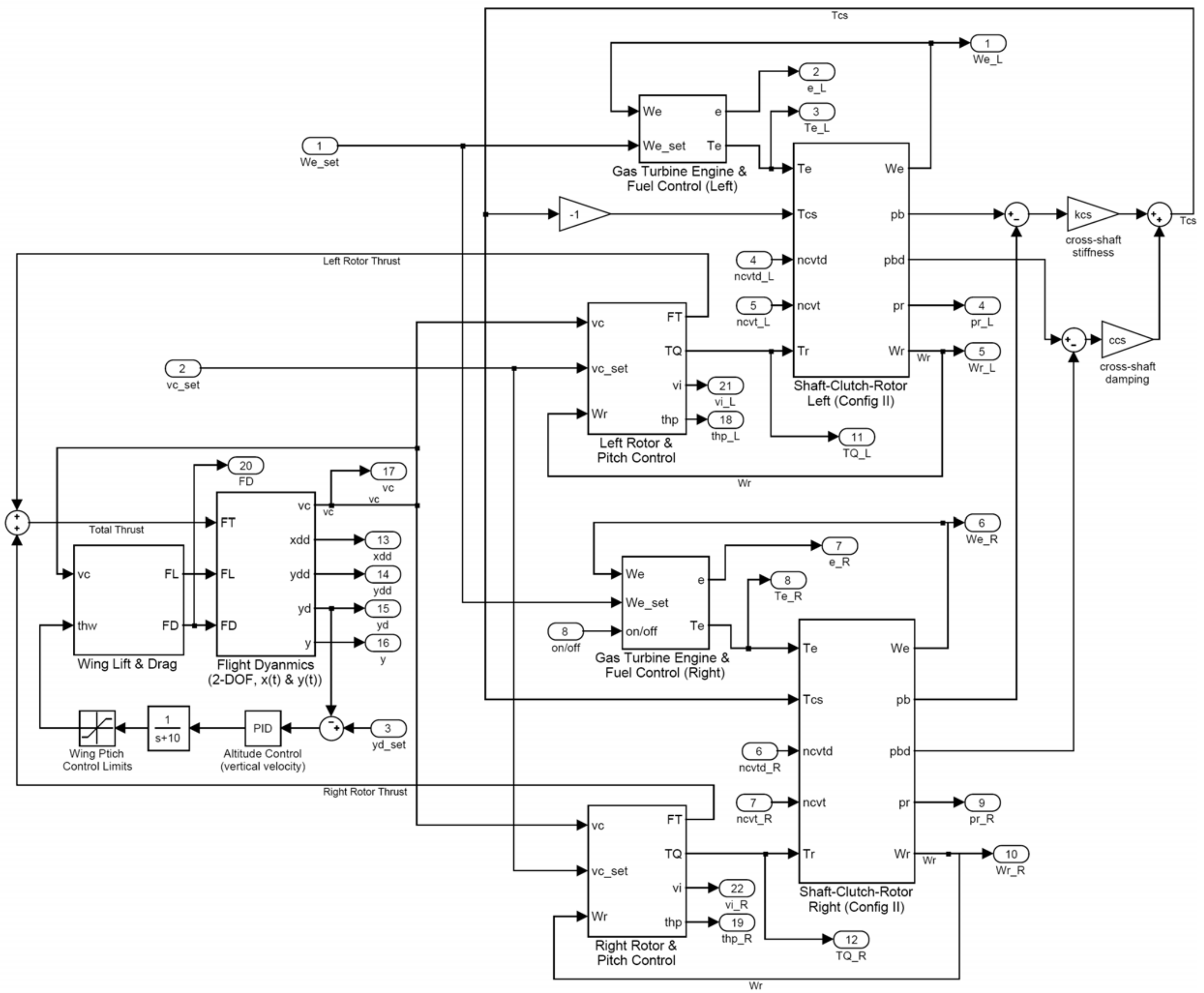
Tcs
1
We_L
2
e_L
3
Te_L
We
e
We_set
Te
Gas Turbine Engine & Fuel Control (Left)
1
We_set
Te
We
-1
Tcs
pb
kcs
cross-shaft stiffness
Tcs
4
ncvtd_L
ncvtd
pbd
5
ncvt_L
ncvt
pr
4
pr_L
ccs
cross-shaft damping
Left Rotor Thrust
vc
FT
TQ
Tr
Wr
Wr
5
Wr_L
2
vc_set
vc_set
vi
21
vi_L
Shaft-Clutch-Rotor Left (Config II)
Wr
thp
18
thp_L
11
TQ_L
Left Rotor & Pitch Control
Wr
20
FD
17
vc
vc
vc
vc
Total Thrust
FT
6
We_R
7
e_R
xdd
13
xdd
We
e
8
Te_R
vc
FL
FL
ydd
14
ydd
We_set
yd
15
yd
8
on/off
on/off
Te
thw
FD
FD
y
16
y
Te
We
Wing Lift & Drag
Flight Dyanmics (2-DOF, x(t) & y(t))
Gas Turbine Engine & Fuel Control (Right)
Tcs
pb
1
s+10
PID
3
yd_set
Wing Ptich Control Limits
Altitude Control (vertical velocity)
6
ncvtd_R
ncvtd
pbd
Right Rotor Thrust
7
ncvt_R
ncvt
pr
9
pr_R
vc
FT
TQ
Tr
Wr
Wr
10
Wr_R
vc_set
vi
22
vi_R
Shaft-Clutch-Rotor Right (Config II)
Wr
thp
19
thp_R
12
TQ_R
Right Rotor & Pitch Control
Wr

Figure B-2.—Two-speed tiltrotor driveline/engine/clutch/rotor/fuel control/flight dynamics block.

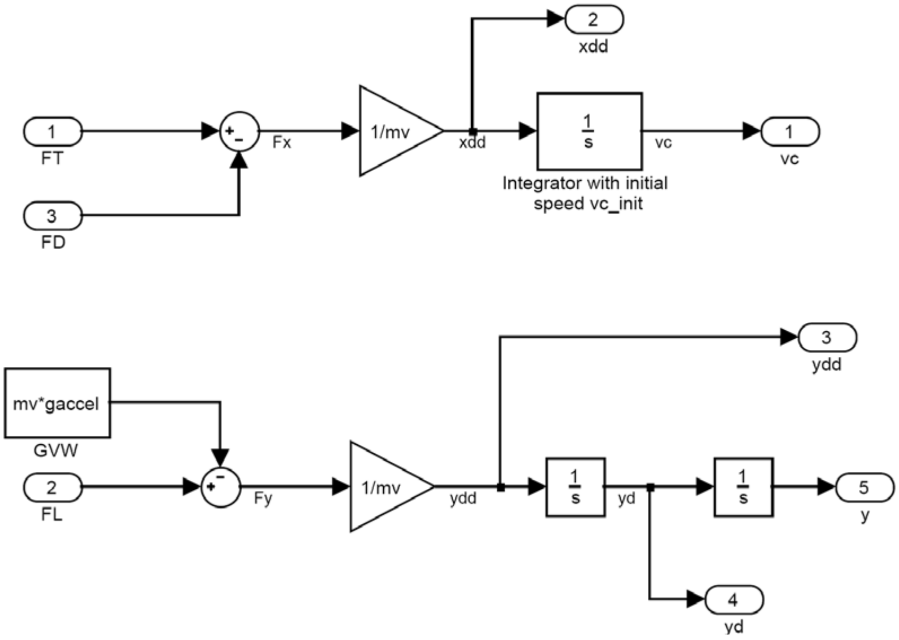

1
FT
3
FD
Fx
1/mv
xdd
2
xdd
1
s
Integrator with initial speed vc_init
vc
1
vc
mv*gaccel
GVW
2
FL
Fy
1/mv
ydd
3
ydd
1
s
yd
1
s
5
y
4
yd

Figure B-3.—Two-DOF (altitude and forward speed) vehicle flight dynamics block.

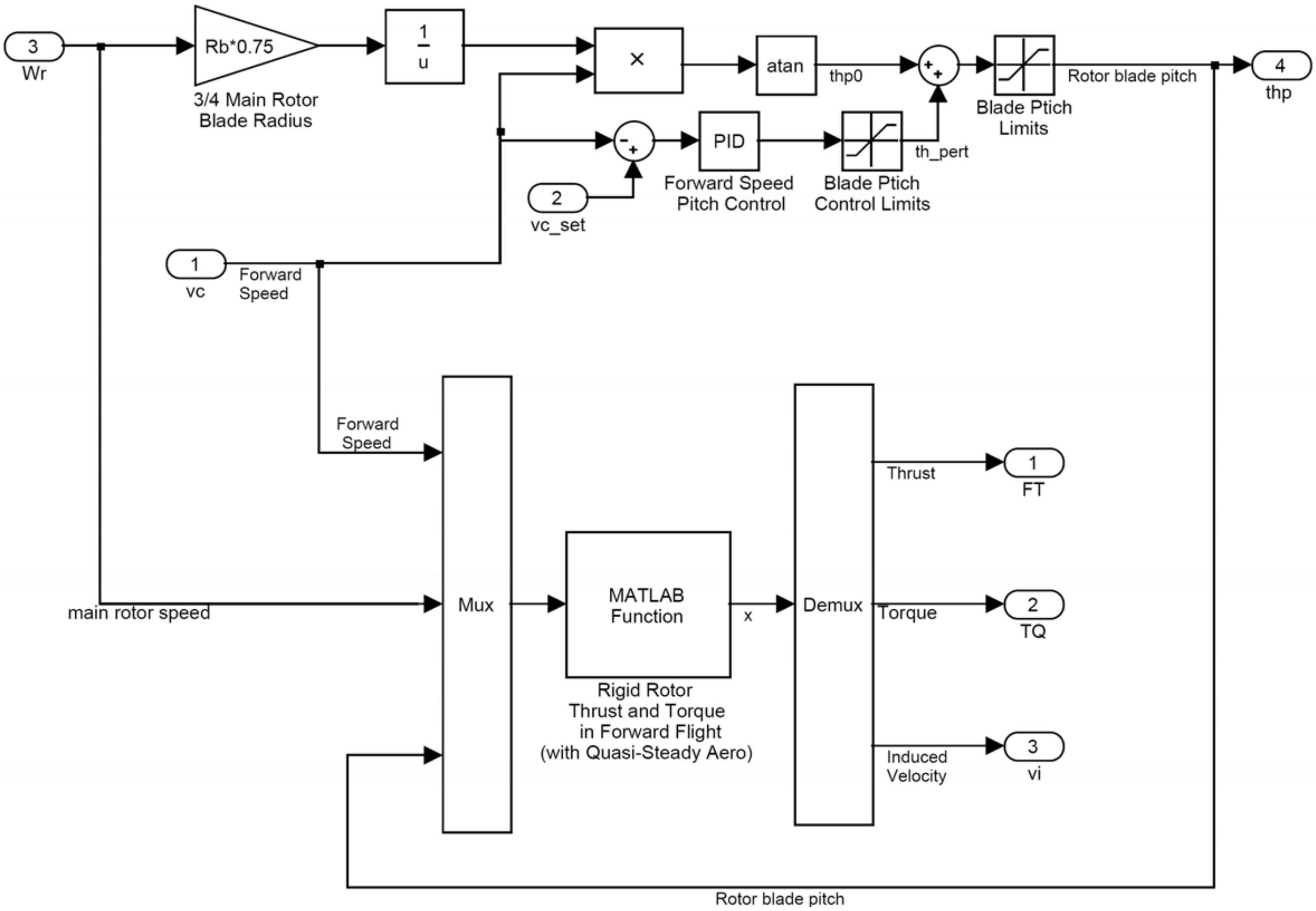

3
Wr
Rb*0.75
3/4 Main Rotor Blade Radius
1
u
×
atan
thp0
Blade Ptich Limits
Rotor blade pitch
4
thp
PID
Forward Speed Pitch Control
Blade Ptich Control Limits
th_pert
2
vc_set
1
vc
Forward Speed
Forward Speed
main rotor speed
Mux
MATLAB Function
Rigid Rotor Thrust and Torque in Forward Flight (with Quasi-Steady Aero)
x
Demux
Thrust
1
FT
Torque
2
TQ
Induced Velocity
3
vi
Rotor blade pitch

Figure B-4.—Rigid rotor and blade pitch forward speed controller block.

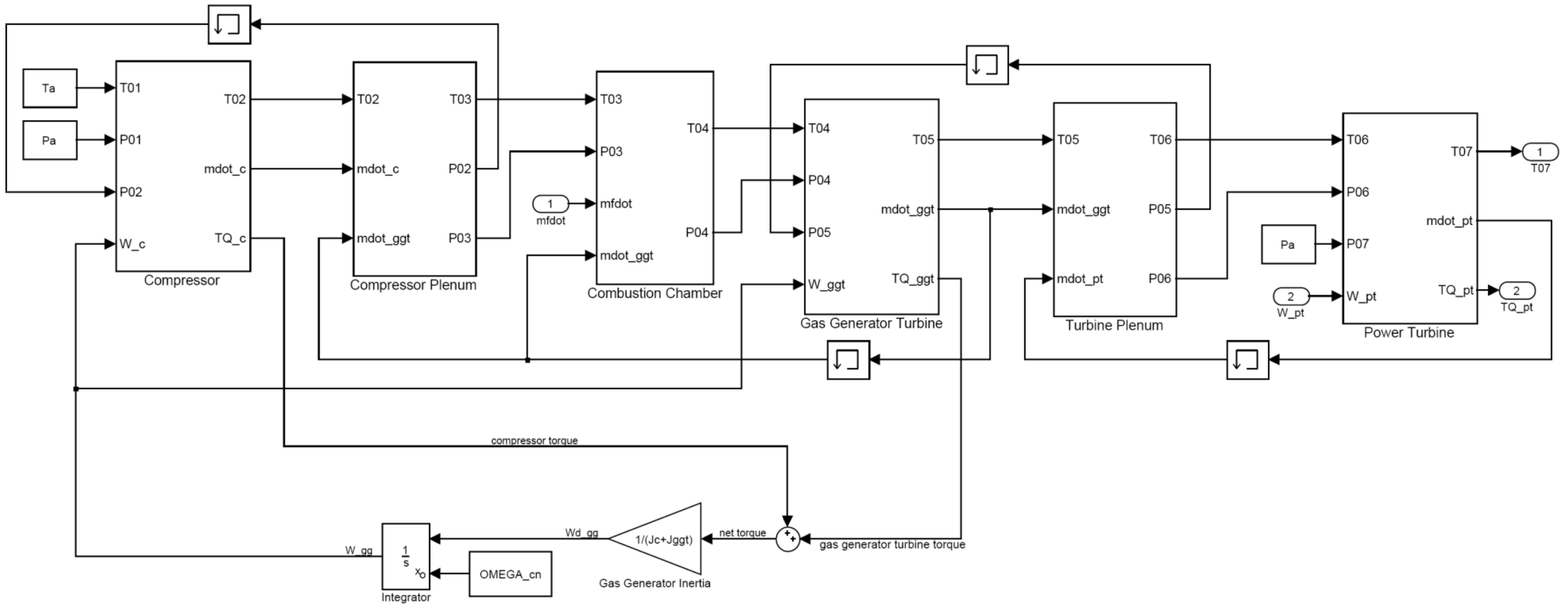
Ta
Pa
T01
P01
P02
W_c
T02
mdot_c
TQ_c
Compressor
T02
mdot_c
mdot_ggt
T03
P02
P03
Compressor Plenum
T03
P03
mfdot
mdot_ggt
T04
P04
1
mfdot
Combustion Chamber
T04
P04
P05
W_ggt
T05
mdot_ggt
TQ_ggt
Gas Generator Turbine
T05
mdot_ggt
mdot_pt
T06
P05
P06
Turbine Plenum
T06
P06
P07
W_pt
T07
mdot_pt
TQ_pt
Power Turbine
Pa
2
W_pt
1
T07
2
TQ_pt
compressor torque
net torque
gas generator turbine torque
1/(Jc+Jggt)
Gas Generator Inertia
Wd_gg
1
s
x_o
Integrator
W_gg
OMEGA_cn

Figure B-5.—Two-spool gas turbine engine simulation block.

REPORT DOCUMENTATION PAGE	*Form Approved* *OMB No. 0704-0188*

The public reporting burden for this collection of information is estimated to average 1 hour per response, including the time for reviewing instructions, searching existing data sources, gathering and maintaining the data needed, and completing and reviewing the collection of information. Send comments regarding this burden estimate or any other aspect of this collection of information, including suggestions for reducing this burden, to Department of Defense, Washington Headquarters Services, Directorate for Information Operations and Reports (0704-0188), 1215 Jefferson Davis Highway, Suite 1204, Arlington, VA 22202-4302. Respondents should be aware that notwithstanding any other provision of law, no person shall be subject to any penalty for failing to comply with a collection of information if it does not display a currently valid OMB control number.
PLEASE DO NOT RETURN YOUR FORM TO THE ABOVE ADDRESS.

1. REPORT DATE *(DD-MM-YYYY)* 01-01-2012	**2. REPORT TYPE** Technical Memorandum	**3. DATES COVERED** *(From - To)*

4. TITLE AND SUBTITLE
Variable-Speed Simulation of a Dual-Clutch Gearbox Tiltrotor Driveline

5a. CONTRACT NUMBER

5b. GRANT NUMBER

5c. PROGRAM ELEMENT NUMBER

6. AUTHOR(S)
DeSmidt, Hans; Wang, Kon-Well; Smith, Edward, C.; Lewicki, David, G.

5d. PROJECT NUMBER

5e. TASK NUMBER

5f. WORK UNIT NUMBER
WBS 877868.02.07.03.01.01.01

7. PERFORMING ORGANIZATION NAME(S) AND ADDRESS(ES)
National Aeronautics and Space Administration
John H. Glenn Research Center at Lewis Field
Cleveland, Ohio 44135-3191

8. PERFORMING ORGANIZATION REPORT NUMBER
E-17891

9. SPONSORING/MONITORING AGENCY NAME(S) AND ADDRESS(ES)
National Aeronautics and Space Administration
Washington, DC 20546-0001

10. SPONSORING/MONITOR'S ACRONYM(S)
NASA

11. SPONSORING/MONITORING REPORT NUMBER
NASA/TM-2012-217212

12. DISTRIBUTION/AVAILABILITY STATEMENT
Unclassified-Unlimited
Subject Category: 37
Available electronically at http://www.sti.nasa.gov
This publication is available from the NASA Center for AeroSpace Information, 443-757-5802

13. SUPPLEMENTARY NOTES

14. ABSTRACT

This investigation explores the variable-speed operation and shift response of a prototypical two-speed dual-clutch transmission tiltrotor driveline in forward flight. Here, a Comprehensive Variable-Speed Rotorcraft Propulsion System Modeling (CVSRPM) tool developed under a NASA funded NRA program is utilized to simulate the drive system dynamics. In this study, a sequential shifting control strategy is analyzed under a steady forward cruise condition. This investigation attempts to build upon previous variable-speed rotorcraft propulsion studies by 1) including a fully nonlinear transient gas-turbine engine model, 2) including clutch stick-slip friction effects, 3) including shaft flexibility, 4) incorporating a basic flight dynamics model to account for interactions with the flight control system. Through exploring the interactions between the various subsystems, this analysis provides important insights into the continuing development of variable-speed rotorcraft propulsion systems.

15. SUBJECT TERMS
Tiltrotor aircraft; Transmission (machine elements); Compressors; Turbines; Clutches

16. SECURITY CLASSIFICATION OF:			**17. LIMITATION OF ABSTRACT**	**18. NUMBER OF PAGES**	**19a. NAME OF RESPONSIBLE PERSON**
a. REPORT U	**b. ABSTRACT** U	**c. THIS PAGE** U	UU	30	STI Help Desk (email:help@sti.nasa.gov) **19b. TELEPHONE NUMBER** ***(include area code)*** 443-757-5802

Standard Form 298 (Rev. 8-98)
Prescribed by ANSI Std. Z39-18